

A Discontinuous Galerkin Method for Ideal Two-Fluid Plasma Equations

J. Loverich, A. Hakim, U. Shumlak

*University of Washington, Aerospace and Energetics Research Program, Seattle,
WA 98195-2250*

Abstract

A discontinuous Galerkin method for the ideal 5 moment two-fluid plasma system is presented. The method uses a second or third order discontinuous Galerkin spatial discretization and a third order TVD Runge-Kutta time stepping scheme. The method is benchmarked against an analytic solution of a dispersive electron acoustic square pulse as well as the two-fluid electromagnetic shock[1] and existing numerical solutions to the GEM challenge magnetic reconnection problem[2]. Results of a two-fluid electrostatic shock are shown which can be used as a simple benchmark for non-neutral two-fluid codes. The algorithm can be generalized to arbitrary geometries and three dimensions.

Key words: Plasma, Two-Fluid, 5 Moment, Discontinuous Galerkin, Electrostatic Shock, Electromagnetic Shock, Magnetic Reconnection

1 Introduction

Fusion power promises to be a safe, efficient and environmentally friendly energy source. Controlled fusion power concepts have been under investigation for decades, the vast majority of these concepts require an intimate understanding of plasma physics to determine the stability and confinement properties. Numerical plasma physics has proved extremely valuable in deciphering experimental data and predicting the behavior of plasma experiments. Many plasma fluid models, and in particular the full two-fluid plasma model, have

* Corresponding author. Address: jlovric@u.washington.edu

¹ Supported by AFOSR Grant No. F49620-02-1-0129. Simulations performed on the Ladon cluster in the department of Mechanical Engineering at the University of Washington.

received very little attention from the numerical plasma physics community. This work describes an advanced algorithm for the ideal 5-moment two-fluid plasma system.

To solve problems in plasma physics and to gain physical intuition of plasma phenomena a hierarchy of classical plasma models have been developed. The most fundamental continuum plasma model is the Vlasov model which eliminates individual particles in favor of a continuous distribution function. This model is six dimensional as the distribution function is a function of both position and velocity. The Vlasov model can be re-written as an equivalent system that consists of an infinite number of moment equations. A reduction of the Vlasov model can then be obtained by truncating this infinite series. Assuming scalar pressure and setting the heat tensor and higher moments to zero produces the 5 moment truncation of the Vlasov model. This model is known as the ideal 5 moment two-fluid plasma model, and will be discussed in this paper. Asymptotic approximations of this two-fluid system produce a series of increasingly simpler fluid models including two-fluid MHD (Magnetohydrodynamics), Hall MHD and then the ideal MHD models.

The main benefit of a fluid model over the Vlasov model is the reduced dimensionality from 6 dimensions to 3 dimensions. Physics is lost in this reduction, but an enormous amount of physics relevant to fusion and spacecraft propulsion remains in the fluid description. Ideal MHD has been extremely successful in explaining large scale instabilities in such devices as the Z-pinch, spheromak and tokamak[3,4]. Unfortunately there are many regimes where the description is invalid and where it fails to explain the observed phenomena. An example of this includes ion demagnetization which is important in Hall thrusters where the plasma is accelerated by the Hall electric field. Hall MHD addresses both these issues but fails to describe other plasma phenomena such as the demagnetization of electrons in regions of low magnetic field which is important in collisionless reconnection. The two-fluid MHD approach adds terms such as electron inertia which is an important mechanism for breaking the frozen in flux condition for electrons as it acts as a “dissipation” mechanism in the absence of resistivity[5]. The quasi-neutrality condition still constrains the electron and ion motions, to allow complete independence of electron and ion motion the quasi-neutrality condition must be relaxed; the result is the ideal two-fluid plasma system.

Two-fluid effects are important in the generation of turbulence through microinstabilities. Most plasmas are turbulent at some scale, however the simplest fluid model, ideal MHD, describes plasmas physics that is more or less laminar where the two-fluid model produces turbulent phenomena. This can be explained in part as a result of the fluid description of electrons. In a two-fluid model both the electrons and the ions may become unstable independently. In particular, electrons carry most of the current in an MHD plasma and this

may produce a large amount of differential motion in the electron fluid when magnetic field gradients are present even if the plasma is in a static MHD equilibrium. The generation of microturbulence through processes such as the lower hybrid drift instability and the modified two-stream instability may be important in both Z-pinch and theta-pinch plasmas and are frequently cited as sources of anomalous resistivity[6], magnetic diffusion and heating and in certain cases may ultimately drive macroscopic MHD instabilities[7].

A particularly good application of the two-fluid plasma model is the fusion Z-pinch. Many plasma experiments last a few seconds whereas the shortest plasma times scale, the electron plasma oscillation, can occur on the scale of pico seconds. However, in the case of the fusion Z-pinch these time scales can be compressed to about 4 orders of magnitude between the shortest time scale, the electron plasma period the MHD instability growth time, which puts two-fluid Z-pinch simulations in the range of numerical methods. Conceptual Z-pinch fusion reactors are high density with extremely strong magnetic fields which makes the two-fluid plasma system particularly applicable [8]. Furthermore the radius of the pinch can be 1000 Debye lengths in some designs [9] which means Debye length scales could be resolved in very high resolution simulations. Artificially increasing the electron mass to ion mass ratio and increasing the ratio of the Alfvén speed to the speed of light can make the Z-pinch problem more computationally tractable while maintaining the relevant physics. The analysis of microinstabilities such as the lower hybrid drift instability may be important in progressing towards a better understanding of Z-pinch physics.

Algorithms have been designed for various fluid plasma models including MHD[10,11], Hall MHD[12–15] various forms of electrostatic two-fluid plasma models[16–18] and the ideal two-fluid system[19,20,1]. The first well described two-fluid plasma algorithm was the ANTHEM[19,20] code. It was used to simulate fast phenomena in high density plasmas inaccessible to PIC codes, the applications included simulations of plasma opening switches and the fast igniter concept. ANTHEM used a flux corrected transport (FCT) type algorithm for the fluids and an FDTD type algorithm for the fields. This type of algorithm is difficult to extend to general geometries because of the staggered scheme used for Maxwell’s equations. In [1] a full two-fluid algorithm using the finite volume method for both fluids and fields was described for one-dimensional problems with the intent of eventually extending the method to multiple dimensions and arbitrary geometries. Unfortunately, it was difficult to extend this algorithm to multiple dimensions because of the divergence errors that develop in the magnetic fields, requiring divergence cleaning. An additional issue was the decay of equilibrium solutions due to the low order of accuracy which resulted from the source term integration and diffusive limiters used. Major improvements on the finite volume technique have been made with the help of various divergence cleaning techniques and careful attention to source term treatment. The finite volume technique is described in

a companion paper[21].

The purpose of the paper is to develop a numerical algorithm for the ideal 5 moment two-fluid plasma system using the discontinuous Galerkin method so that it can be easily generalized to arbitrary geometries and to arbitrarily high order accuracy to help capture plasma instabilities. TVB discontinuous Galerkin methods are described in [22–24]. They are extended to the multi-dimensional Euler equations in [25] and to Maxwell’s equations in [26,27]. The two-fluid system of equations consists of two sets of Euler equations, one for the electrons and the other for the ions, and the complete Maxwell’s equations. The ideal two-fluid system differs from the ideal MHD equations in that it is composed of three separate (but well understood) hyperbolic systems coupled through source terms. The MHD equations are, on the other hand, a unique hyperbolic system. A discontinuous Galerkin method for the MHD equations was developed in [28] and it is used in a Vlasov-Maxwell algorithm in [29], numerous other applications can be found in [30].

In section 2 the ideal 5-moment two-fluid model is described and the equations are presented. In section 3 a scalar model problem is derived from the two-fluid systems which helps to illustrate some of the numerical issues with the system. In section 4 the discontinuous Galerkin method applied to the two-fluid plasma system is presented. In section 5 simulations are presented including an electron acoustic pulse for validation of code accuracy, an electrostatic shock, the two-fluid electromagnetic shock[1], and the GEM challenge magnetic reconnection problem[2] where the reconnected magnetic flux can be compared to published results. Finally, in section 6 the conclusions are discussed.

2 Two-Fluid Model

The full two-fluid plasma model consists of a set of fluid equations for the electrons and ions plus the complete Maxwell’s equations including displacement current. The fluid and electromagnetic systems are coupled by Lorentz forces and current sources. In the following equations, \mathbf{E} is the electric field, \mathbf{B} is the magnetic field, q_s is the species charge (subscript s is i for ions and e for electrons), ρ_s is the species density, m_s is the species mass, \mathbf{U}_s is the species velocity, P_s is the species pressure and e_s is the species total energy with $e_s = \frac{1}{2}\rho_s \mathbf{U}_s^2 + \frac{1}{1-\gamma_s}p_s$. The species number density is defined as $n_s = \frac{\rho_s}{m_s}$, ϵ_0 is the permittivity and μ_0 is the permeability of free space. The complete Ampere’s law is used

$$\partial_t \mathbf{E} - c^2 (\nabla \times \mathbf{B}) = -\frac{1}{\epsilon_0} \sum_s \frac{q_s}{m_s} \rho_s \mathbf{U}_s, \quad (1)$$

and the complete Faraday's law

$$\partial_t \mathbf{B} + (\nabla \times \mathbf{E}) = 0. \quad (2)$$

The magnetic flux equation,

$$\nabla \cdot \mathbf{B} = 0 \quad (3)$$

and Poisson's equation (4),

$$\nabla \cdot \mathbf{E} = \frac{1}{\epsilon_0} (q_i n_i + q_e n_e) \quad (4)$$

are constraint equations which can be derived from Ampere's law (1) and Faraday's law (2). The constraints are not solved numerically which can be problematic [31], however, errors in divergence do not effect the results described in this paper.

The fluid equations are simply the inviscid Navier Stokes equations with Lorentz force source terms. Each fluid species has its own equation for energy,

$$\partial_t e_s + \nabla \cdot (\mathbf{U}_s (e_s + P_s)) = \frac{q_s}{m_s} \rho_s \mathbf{E} \cdot \mathbf{U}_s, \quad (5)$$

momentum,

$$\partial_t (\rho_s \mathbf{U}_s) + \nabla_\alpha (\rho_s \mathbf{U}_s^\alpha \mathbf{U}_s) + \nabla_\alpha (\delta^{\alpha\beta} P_s) = \frac{q_s}{m_s} \rho_s (\mathbf{E} + \mathbf{U}_s \times \mathbf{B}), \quad (6)$$

and continuity,

$$\partial_t \rho_s + \nabla \cdot (\rho_s \mathbf{U}_s) = 0. \quad (7)$$

This means that each species has its own temperature, velocity and number density. As a result, quasi-neutrality is not assumed and things like electron plasma waves and ion subshocks should be observed numerically. This system is identical to the system used in [1].

The ideal two fluid plasma system can be written as three systems of balance laws,

$$\frac{\partial Q_e}{\partial t} + \nabla \cdot F_e(Q_e) = \psi_e(Q_e, Q_{em}), \quad (8)$$

for the electron equations,

$$\frac{\partial Q_i}{\partial t} + \nabla \cdot F_i(Q_i) = \psi_i(Q_i, Q_{em}), \quad (9)$$

for the ion equations, and

$$\frac{\partial Q_{em}}{\partial t} + \nabla \cdot F_{em}(Q_{em}) = \psi_{em}(Q_i, Q_e), \quad (10)$$

for Maxwell's equations. These balance laws, Eqns.(8)-(10), are given in full form by,

$$\frac{\partial}{\partial t} \begin{pmatrix} \rho_s \\ \rho_s U_{xs} \\ \rho_s U_{ys} \\ \rho_s U_{zs} \\ e_s \end{pmatrix} + \nabla \cdot \begin{pmatrix} \rho_s U_{xs} & \rho_s U_{ys} & \rho_s U_{zs} \\ \rho_s U_{xs} U_{xs} + P_s & \rho_s U_{xs} U_{ys} & \rho_s U_{xs} U_{zs} \\ \rho_s U_{ys} U_{xs} & \rho_s U_{ys} U_{ys} + P_s & \rho_s U_{ys} U_{zs} \\ \rho_s U_{zs} U_{xs} & \rho_s U_{zs} U_{ys} & \rho_s U_{zs} U_{zs} + P_s \\ U_{xs} (e_s + P_s) & U_{ys} (e_s + P_s) & U_{zs} (e_s + P_s) \end{pmatrix} = \begin{pmatrix} 0 \\ q_s n_s (E_x + U_{ys} B_z - U_{zs} B_y) \\ q_s n_s (E_y + U_{zs} B_x - U_{xs} B_z) \\ q_s n_s (E_z + U_{xs} B_y - U_{ys} B_x) \\ q_s n_s (E_x U_{xs} + E_y U_{ys} + E_z U_{zs}) \end{pmatrix} \quad (11)$$

$$\frac{\partial}{\partial t} \begin{pmatrix} B_x \\ B_y \\ B_z \\ E_x \\ E_y \\ E_z \end{pmatrix} + \nabla \cdot \begin{pmatrix} 0 & E_z & -E_y \\ -E_z & 0 & E_x \\ E_y & -E_x & 0 \\ 0 & -c^2 B_z & c^2 B_y \\ c^2 B_z & 0 & -c^2 B_x \\ -c^2 B_y & c^2 B_x & 0 \end{pmatrix} = \begin{pmatrix} 0 \\ 0 \\ 0 \\ -\frac{1}{\epsilon_0} (q_e n_e U_{xe} + q_i n_i U_{xi}) \\ -\frac{1}{\epsilon_0} (q_e n_e U_{ye} + q_i n_i U_{yi}) \\ -\frac{1}{\epsilon_0} (q_e n_e U_{ze} + q_i n_i U_{zi}) \end{pmatrix} \quad (12)$$

3 Derivation of a Scalar Model Problem

The ideal 5-moment two-fluid system is unusual in that the source terms act as harmonic oscillators, the source terms are purely dispersive without dissipation

or amplification. This fact is important when considering numerical methods to use, as the source term integration should introduce as little dissipation as feasible in order to avoid damping these oscillations. It frequently occurs in a two-fluid plasma that convective forces are in balance with oscillating sources to produce an equilibrium. With this in mind, a simple model problem is derived which may help one choose a proper numerical method for the two-fluid system.

Linearizing the electron x-momentum equation (6) and Ampere's law (1) while assuming a constant background ion density and assuming that $\mathbf{B} = 0$, a partial differential equation for electron plasma oscillations can be derived which takes the form

$$\frac{\partial^2 u}{\partial t^2} = -\omega_{pe}^2 u, \quad (13)$$

where u is the perturbed x velocity and ω_{pe} is the electron plasma frequency. This can be transformed to a first order equation in complex variables by making the transformation $\omega_{pe} v = \frac{\partial u}{\partial t}$ and letting $Q = v + i u$.

$$\frac{\partial Q}{\partial t} = i \omega_{pe} Q. \quad (14)$$

By transforming variables $u(x, t) \rightarrow u(x + at, t)$ Equation(14) becomes an advection oscillation equation

$$\frac{\partial Q}{\partial t} + a \frac{\partial Q}{\partial x} = i \omega_{pe} Q, \quad (15)$$

where a is the wave propagation speed and ω_{pe} is the oscillation frequency. Any algorithm that is stable to the two-fluid system should be stable when applied to Eqn(15). This equation has solutions $Q = A e^{i(kx - \omega t)}$ where $\omega = a k - \omega_{pe}$. In particular(15) admits a steady state solution $Q = A e^{i k x}$ on an infinite domain where the source term is in balance with the flux. It is important to note that there are an infinite number of equilibria which differ by a continuous range of scalar factors A . This point is important when considering numerical methods for this system since a numerical method with too much dissipation could conceivably move a steady state solution from one equilibrium to another all the while moving towards a state where $A = 0$. This loss of amplitude is also observed in equilibrium type problems in the two-fluid system. An effective numerical algorithm must be both stable to the advection equation and oscillation equation and must have low dissipation in equilibrium type problems. The discontinuous Galerkin method is an ideal candidate for solving the two-fluid system since its accuracy can easily be increased to reduce numerical dissipation while being stable to both the advection equation and the oscillation equation.

4 Runge-Kutta Discontinuous Galerkin Method

Discontinuous Galerkin methods are high order extensions of upwind schemes using a finite element formulation where the elements are discontinuous at cell interfaces. Details of the method are discussed in [22–25] and reproduced here for our particular case. The balance law

$$\frac{\partial Q}{\partial t} + \nabla \cdot F(Q) = \psi(Q) \quad (16)$$

is multiplied by the set of basis functions $\{v_r\}$ and integrated over the finite volume element K . For second order spatial accuracy the basis set

$$\{v_r\} = \{v_0, v_x, v_y\} = \left\{1, \frac{x - x_{ij}}{\frac{1}{2}\Delta x}, \frac{y - y_{ij}}{\frac{1}{2}\Delta y}\right\} \quad (17)$$

is used and for third order spatial accuracy

$$\{v_r\} = \{v_0, v_x, v_y, v_{xy}, v_{xx}, v_{yy}\} = \left\{1, v_x, v_y, v_x v_y, v_x^2 - \frac{1}{3}, v_y^2 - \frac{1}{3}\right\} \quad (18)$$

is used. The equation is written,

$$\int_K \frac{\partial Q}{\partial t} v_r dV + \int_K (\nabla \cdot F) v_r dV = \int_K \psi v_r dV. \quad (19)$$

Integrate by parts to get

$$\int_K \frac{\partial Q}{\partial t} v_r dV + \int_{\partial K} (F \cdot n) v_r d\Gamma - \int_K F \cdot (\nabla v_r) dV = \int_K \psi v_r dV. \quad (20)$$

The discrete conserved variable Q is defined as a linear combination of the basis functions inside an element K , with

$$Q = \sum_r v_r Q_r. \quad (21)$$

The integral $\int_K \frac{\partial Q}{\partial t} v_r dV = \frac{\partial Q_r}{\partial t} C V$ where C is the constant $\frac{1}{V} \int_K v_r^2 dV$ and V is the volume of the element. Using these definitions we get the discrete equation

$$\frac{\partial Q_r}{\partial t} C V + \sum_e \sum_l w_l (F \cdot n) v_r \Gamma_e - \sum_m w_m F \cdot (\nabla v_r) V = \sum_m w_m \psi v_r V, \quad (22)$$

when the integrals are replaced by appropriate Gaussian quadratures. Γ_e is the surface area of the cell face in consideration, e refers to an element face, l are quadrature points on a face, w_l the associated weight and m are quadrature points in the volume with w_m the associated weight. For a second order method

the edge integrals are replaced by a two point Gaussian quadrature

$$\int_{-1}^1 f(x) dx \approx f\left(\frac{1}{\sqrt{3}}\right) + f\left(-\frac{1}{\sqrt{3}}\right) \quad (23)$$

A four point quadrature is used for the volume integral given by,

$$\int_{-1}^1 \int_{-1}^1 f(x, y) dx dy \approx f\left(\frac{1}{\sqrt{3}}, \frac{1}{\sqrt{3}}\right) + f\left(-\frac{1}{\sqrt{3}}, \frac{1}{\sqrt{3}}\right) + f\left(-\frac{1}{\sqrt{3}}, -\frac{1}{\sqrt{3}}\right) + f\left(\frac{1}{\sqrt{3}}, -\frac{1}{\sqrt{3}}\right). \quad (24)$$

The discrete equations for the second order scheme are

$$\frac{\partial Q_0}{\partial t} V + \sum_e \sum_l w_l (F \cdot n) v_0 \Gamma_e = \sum_m w_m \psi v_0 V, \quad (25a)$$

$$\frac{\partial Q_x}{\partial t} V + 3 \sum_e \sum_l w_l (F \cdot n) v_x \Gamma_e - 3 \sum_m w_m F \cdot (\nabla v_x) V = 3 \sum_m w_m \psi v_x V, \quad (25b)$$

$$\frac{\partial Q_y}{\partial t} V + 3 \sum_e \sum_l w_l (F \cdot n) v_y \Gamma_e - 3 \sum_m w_m F \cdot (\nabla v_y) V = 3 \sum_m w_m \psi v_y V. \quad (25c)$$

The derivatives of the basis functions can be calculated analytically since the polynomial basis functions are known. The discontinuous Galerkin method is applied to each balance law (8)(9)(10) at every time step. For the third order space method the edge integrals are done using a 3 point quadrature

$$\int_{-1}^1 f(x) dx \approx \frac{8}{9} f(0) + \frac{5}{9} \left(f\left(\frac{\sqrt{3}}{5}\right) + f\left(-\frac{\sqrt{3}}{5}\right) \right) \quad (26)$$

The volume integrals are performed using a 9 point quadrature which can be calculated by doing a 3 point integration in the x direction and then a 3 point integration in the y direction. This produces the following approximate integral

$$\begin{aligned} \int_{-1}^1 \int_{-1}^1 f(x, y) dx dy \approx & \frac{64}{81} f(0, 0) + \\ & \frac{25}{81} \left[f\left(\frac{\sqrt{3}}{5}, \frac{\sqrt{3}}{5}\right) + f\left(-\frac{\sqrt{3}}{5}, \frac{\sqrt{3}}{5}\right) + f\left(-\frac{\sqrt{3}}{5}, -\frac{\sqrt{3}}{5}\right) + f\left(\frac{\sqrt{3}}{5}, -\frac{\sqrt{3}}{5}\right) \right] + \\ & \frac{40}{81} \left[f\left(0, \frac{\sqrt{3}}{5}\right) + f\left(\frac{\sqrt{3}}{5}, 0\right) + f\left(0, -\frac{\sqrt{3}}{5}\right) + f\left(-\frac{\sqrt{3}}{5}, 0\right) \right] \quad (27) \end{aligned}$$

For the 3rd order scheme the following discrete equations must be updated in addition to those given by the second order scheme(25)

$$\frac{\partial Q_{xy}}{\partial t} V + 9 \sum_e \sum_l w_l (F \cdot n) v_{xy} \Gamma_e - 9 \sum_m w_m F \cdot (\nabla v_{xy}) V = 9 \sum_m w_m \psi v_{xy} V, \quad (28a)$$

$$\frac{\partial Q_{xx}}{\partial t} V + \frac{45}{4} \sum_e \sum_l w_l (F \cdot n) v_{xx} \Gamma_e - \frac{45}{4} \sum_m w_m F \cdot (\nabla v_{xx}) V = \frac{45}{4} \sum_m w_m \psi v_{xx} V, \quad (28b)$$

$$\frac{\partial Q_{yy}}{\partial t} V + \frac{45}{4} \sum_e \sum_l w_l (F \cdot n) v_{yy} \Gamma_e - \frac{45}{4} \sum_m w_m F \cdot (\nabla v_{yy}) V = \frac{45}{4} \sum_m w_m \psi v_{yy} V. \quad (28c)$$

Though the spatial discretization uses a finite element approach, the time integration uses standard finite difference methods which are described in the next section. The algorithm described is an explicit finite element method, data is only exchanged between neighboring cells. The solution does not need to be continuous at cell interfaces which is particularly useful for problems with shocks.

4.1 Time Integration Schemes

Time integration schemes that are stable for the advection equation must also be stable to the oscillation equation if they are to be stable in general to the two-fluid system. Two time integration schemes that are stable to the oscillation equation and that work well with the discontinuous Galerkin method are as follows, the 3rd order TVD Runge-Kutta method[22],

$$Q^1 = Q^n + \Delta t L [Q^n] \quad (29a)$$

$$Q^2 = \frac{3}{4} Q^n + \frac{1}{4} (Q^1 + \Delta t L [Q^1]) \quad (29b)$$

$$Q^{n+1} = \frac{1}{3} Q^n + \frac{2}{3} (Q^2 + \Delta t L [Q^2]), \quad (29c)$$

and the standard 4th order Runge-Kutta method [32]

$$k_1 = \Delta t L [Q^n] \quad (30a)$$

$$k_2 = \Delta t L \left[Q^n + \frac{1}{2} k_1 \right] \quad (30b)$$

$$k_3 = \Delta t L \left[Q^n + \frac{1}{2} k_2 \right] \quad (30c)$$

$$k_4 = \Delta t L [Q^n + k_3] \quad (30d)$$

$$Q^{n+1} = Q^n + \frac{1}{6} (k_1 + 2 k_2 + 2 k_3 + k_4). \quad (30e)$$

The time integration scheme is applied to each Q_r at every time step to evolve the solution. The term $L [Q^n]$ represents the entire “left hand side” which is everything but the time derivative evaluated at Q^n . It is important to note that all two step second order Runge-Kutta schemes are unstable to the oscillation equation[32]. In this paper, the results presented use the 3rd order TVD Runge-Kutta method.

4.2 Evaluating $F \cdot n$

The flux $F \cdot n$ can be evaluated a number of different ways. Both approximate Riemann solvers and the Lax flux have been used. For the 3rd order discontinuous Galerkin method for the two-fluid system the local Lax flux is more robust and so it is used throughout this paper. The local Lax flux at each face is calculated as

$$F \cdot n = \frac{1}{2} (F_i^+ + F_{i+1}^-) \cdot n - \frac{1}{2} |\lambda|_{i+1/2} (Q_i^+ - Q_{i+1}^-) \cdot n, \quad (31)$$

where $|\lambda|_{i+1/2}$ is the maximum eigenvalue of the particular system based on the averages, Q_0 , of the conserved variables at the centers of cell i and $i+1$. The local Lax flux is a well known flux function that can be used in the discontinuous Galerkin method [22]. For the fluid systems $|\lambda|_{i+1/2} = \left(|u_\alpha| + \left(\gamma_\alpha \frac{p_\alpha}{\rho_\alpha} \right)^{\frac{1}{2}} \right)_{i+1/2}$ is used. This choice of the eigenvalue is important for the fluid equations because it frequently happens for the two-fluid system that conserved variable values at the interface produce imaginary sound speeds whereas this occurs much less often for the conserved variables at the center of each cell. Imaginary sound speeds typically become more of a problem as the grid resolution is increased. This is partly attributed to the overall decrease in numerical diffusion of the high frequency waves. Increased spatial resolution and temporal resolution results in larger and higher frequency physical oscillations in the source terms and the results are prone to negative pressures, particularly in the 3rd order discretization, perhaps due to the non-conservative form of the algorithm. It has been found that the local Lax flux alleviates this problem by introducing more dissipation so that negative pressure occurs much less often, even as the grid resolution is increased. For Maxwell’s equations $|\lambda| = c$. The superscripts $+$ and $-$ mean that the Q is evaluated at the upper or lower edge of the cell.

The local Lax flux is diffusive. Less diffusive fluxes such as an approximate Riemann flux can be used. The local Lax flux has several advantages over the Riemann flux. First of all it is simpler to implement and can be used as a base scheme when testing higher moment fluid equations such as the 10, 20 or 35 moment fluid equations which correspond to gyroviscous fluid models; the eigensystems for these models are complex and using a local Lax flux simplifies

the implementation. Also, note that the local Lax flux was used in the original multi-dimensional Euler discontinuous Galerkin algorithm [25] and it is logical to extend that work by using the local Lax flux as our base flux. In general it has been observed that a Riemann flux gives a similar quality solution at roughly half the resolution of a local Lax flux using the second order scheme. Of course, the use of a local Lax flux reduces overall energy conservation for a given grid resolution, but this problem is alleviated by increasing resolution. It has been suggested that as the order of the polynomial representation is increased the choice of flux function, “does not have a significant impact on the quality of the approximations” [33].

We have observed that the local Lax flux has better divergence properties for Maxwell’s equations with source terms than the approximate Riemann flux. Large grid aligned divergence errors occur when using a Riemann flux unless the constant M in the TVB limiter, discussed in section 4.3, is set to a non-zero value. When the local Lax flux is used $M = 0$ produces significantly smaller grid aligned divergence errors. In conclusion, the local Lax flux for the two-fluid plasma system is more robust than an approximate Riemann flux, simpler to implement, does not suffer precision errors that arise during the Riemann decomposition, does not suffer large grid aligned $\nabla \cdot B$ errors to the extent that an approximate Riemann flux does when limiters are applied (limiters need to be applied to Maxwell’s equations otherwise they can induce negative pressure errors in the fluid equations), and is easy to apply to more complex fluid and electromagnetic systems; for these reasons the local Lax flux is attractive and is used in the simulations that follow.

4.3 Limiting

High resolution schemes typically use limiting to prevent spurious oscillations near discontinuities and for stabilization of non-linear systems[34]. Limiters can also be used in the discontinuous Galerkin method, though instead of being TVD, minmod limiters produce a scheme that is TVDM or TVD in the mean. This means that the solution is TVD in Q_0 , but not necessarily in Q .

Following the procedure described in [23] the conserved variables Q can be limited in terms of characteristics or in terms of components. To limit Q in terms of characteristics the Q are first transformed to characteristic variables g where $g = LQ$ and L is the left eigenvector matrix of the flux Jacobian calculated from Q_0 . The left eigenvector matrix is also applied to the differences $L(Q_0^{i+1} - Q_0^i) = \Delta^+ g_0$ and $L(Q_0^i - Q_0^{i-1}) = \Delta^- g_0$. Limiting is performed directly on transformed variables and then the solution is immediately trans-

formed back to determine the limited form of Q_x ,

$$\bar{Q}_x = L^{-1} m \left(g_x, \Delta^+ g_0, \Delta^- g_0 \right) \quad (32)$$

where m is the minmod limiter defined by

$$m(a, b, c) = \begin{cases} \max(a, b, c) & \text{if } \text{sign}(a) = \text{sign}(b) = \text{sign}(c) = - \\ \min(a, b, c) & \text{if } \text{sign}(a) = \text{sign}(b) = \text{sign}(c) = + \\ 0 & \text{otherwise} \end{cases} \quad (33)$$

The minmod limiter Eqn. (33) is used for each of the fluid equations Eqn.(8)(9) while if the simulation is 2D a modified minmod limiter is used on Maxwell's equations Eqn.(10) so that divergence errors in the B field are reduced. The modified minmod limiter is

$$\bar{m}(a, b, c) = \begin{cases} a & \text{if } |a| < M dx^2 \\ m(a, b, c) & \text{otherwise} \end{cases}, \quad (34)$$

where M is a constant. Component limiting is done in a similar manner except no transformation is necessary, so that the limiter is directly applied to the variables Q . Component limiting has the advantage that it is faster than characteristic limiting and it does not introduce machine precision errors that can result during the transformation $Q = L^{-1}(LQ)$. Although analytically the transformation is exact, numerically precision errors are introduced which can be large if large numbers are added to small numbers. The issue of precision errors is especially important for the third order space DG method. Unfortunately component limiting is not TVDM[23].

When a 3rd order DG method is used, two types of limiters can be used. The first method follows the procedure of second order method and is described in [24] where if $\bar{Q}_x \neq Q_x$ then all higher order coefficients are set to zero. This method is simple to implement and is used in this paper.

A different and potentially better 3rd order limiter is that of [35]. In this method, the linear terms, Q_x , Q_y , Q_z are limited in the same way as the second order method while the higher order terms Q_{xy} , Q_{xx} and Q_{yy} are limited as follows.

$$\bar{Q}_{xx}^i = m \left[Q_{xx}^i, \frac{1}{2} (Q_x^{i+1} - Q_x^i), \frac{1}{2} (Q_x^i - Q_x^{i-1}) \right] \quad (35)$$

and

$$\bar{Q}_{yy}^j = m \left[Q_{yy}^j, \frac{1}{2} (Q_y^{j+1} - Q_y^j), \frac{1}{2} (Q_y^j - Q_y^{j-1}) \right] \quad (36)$$

finally, the term Q_{xy} is limited by setting it to zero if either Q_{xx} or Q_{yy} is limited. In [24] it was suggested that the high order terms could be limited by simply setting them to zero if the linear terms are limited. The justification is

that oscillations in the higher order terms would only be important when oscillations in the linear terms exist. Limiting the higher order terms independent of the limiting of the lower order terms (as just described) is found to reduce errors associated with machine precision. This may be due to significant oscillations developing in the higher order terms when they are not present in the lower order terms. Unfortunately, despite producing more symmetric solutions early in time for simulations of the GEM challenge reconnection problem (to be described in section 5), late in time, this method frequently leads to the development of negative pressures that are difficult to correct.

4.4 Stability

The stability limits of the numerical algorithm just described are defined by the highest oscillation frequency of the system or by the CFL condition based on the speed of light. Typically the highest oscillation frequency is the electron plasma frequency $w_{pe} = \left(\frac{n_e q_e^2}{\epsilon_0 m_e}\right)^{\frac{1}{2}}$ and a time step is chosen for which the time integration scheme is stable to this frequency of oscillation, this time step is typically $\Delta t < \frac{1}{w_{pe}}$. When the CFL condition dominates the time step $\Delta t < \frac{1}{6} \frac{\Delta x}{c}$ is used for the second order spatial discretization in 2D and $\Delta t < \frac{1}{10} \frac{c}{\Delta x}$ for the third order spatial discretization in 2D.

4.5 Divergence errors

Divergence errors are a common problem in plasma codes and techniques for solving these issues have been discussed in detail for magnetohydrodynamics codes in [36]. Ultimately divergence cleaning will need to be applied to the two-fluid plasma algorithm. However, our experience has shown that the discontinuous Galerkin method applied to the two-fluid plasma system works quite well without divergence cleaning in cases where a finite volume code (developed in parallel) fails completely.

Two techniques have been applied to the finite volume method that can also be applied to the discontinuous Galerkin algorithm for the two-fluid system. The first method solves the potential form of Maxwell's equations re-written as a system of 16 first order equations. In this case, both divergence constraints are satisfied automatically though a new constraint, the Lorentz gauge condition for example, arises. Since the gauge condition is first order, gauge cleaning may be performed algebraically for each cell. A second approach to divergence cleaning, which has been used successfully by the authors in the the finite volume code, is to use the perfectly hyperbolic Maxwell's equations as described in [37]. Both these techniques are hyperbolic divergence cleaning techniques

so they can be applied to the described algorithm simply by changing Q_{em} , F_{em} and ψ_{em} if Lax fluxes and componentwise limiting is used. If Riemann fluxes or characteristic limiting is used then the eigensystems of the new electromagnetic systems would also need to be calculated.

In MHD codes large divergence errors can occur at shocks, in the two-fluid plasma system this is not such an issue since true shocks do not occur in the magnetic field. For most situations, true shocks only occur in the ion fluid, followed by a smooth Debye length transition in the electron quantities and then a broader transition in the magnetic field profile. Finally, the results of this research have benefited from the parallel development of a divergence cleaned finite volume two-fluid code [21] so that results could be compared.

5 Simulations

The two-fluid system describes many dispersive waves including the electron acoustic wave. In a plasma the electron acoustic wave is coupled to the plasma frequency producing a wave that is essentially stationary for sufficiently long wavelengths or sufficiently cold plasmas. In the following a dispersion relation for the electron acoustic wave in a warm plasma is derived from linearized two-fluid equations. The dispersion relation is used to calculate an analytic solution to the propagation of an approximate square pulse in a two-fluid plasma. The numerical two-fluid solution using the 2nd and 3rd order discontinuous Galerkin method is compared to the analytic solution using various grid resolution and the order accuracy of the algorithm in the L_2 norm is calculated.

Assume infinitely massive ions with a background number density n_0 for both electrons and ions and charge $q_i = -q_e$. Furthermore, assume background electron and ion pressures P_0 while all other background quantities are zero. A perturbed electron velocity $u_e^1 = U_0 e^{i(k_n x + w_n t)}$ is assumed. Corresponding perturbed electric field, density and pressure profiles can be derived from Poisson's equation, the continuity equation and the energy equation so that the perturbed electric field $E_{x n}^1 = \frac{i}{\epsilon_0 w_n} n_0 q_e u_e^1$, perturbed electron pressure, $P_{e n}^1 = -\left(\frac{k_n}{w_n}\right) \gamma_e P_0 u_e^1$, and perturbed electron density, $\rho_{e n}^1 = -\left(\frac{k_n}{w_n}\right) \rho_{0 e} u_e^1$. The electron acoustic dispersion relation is

$$w_n = \pm \left[\left(\frac{\gamma_e P_0}{\rho_{0 e}} \right) k_n^2 + \left(\frac{n_0 q_e^2}{\epsilon_0 m_e} \right) \right]^{\frac{1}{2}}. \quad (37)$$

Taking the positive root waves that travel to the left are defined. A square pulse on a periodic domain is defined by taking linear combinations of these

waves,

$$u_e^1(x, t) = -U_0 \sum_{n=0}^{\infty} \frac{i}{2n+1} e^{i(k_n x + w_n t)}. \quad (38)$$

As a practical matter, an approximate square pulse is used since the high wave numbers cannot be resolved numerically unless the spatial resolution is sufficiently high. Figures 1 and 2 illustrate this dramatically. Figure 1 shows the initial square pulse initialized with 5000 wave modes. Figure 1 shows the analytic solution after $t = 1000$ steps. Since there is no dissipation in the system and the system is dispersive the high frequency modes in the initial conditions play an important role in the final solution; this makes the issue of convergence in shock-type problems that start out with discontinuities difficult to assess. As a result, in the simulations and analytic solutions that follow, $n = 9$ is the highest mode included in the expansion and $k_n = 2\pi n$. Finally, only the real part of all perturbed quantities are used in the initial conditions, thus,

$$E_x^1(x, t) = \sum_{n=0}^9 E_{xn}^1 \quad (39)$$

$$P_e^1(x, t) = \sum_{n=0}^9 P_{en}^1 \quad (40)$$

$$\rho_e^1(x, t) = \sum_{n=0}^9 \rho_{en}^1 \quad (41)$$

In this simulation $q_i = -q_e = 10$, $\epsilon_0 = 1$, $n_0 = 1$, $P_0 = 1$, $m_e = 1$, $m_i = \infty$, $\gamma_e = 2$ for convenience. To ensure that the solution is in the linear regime U_0 must be set to a small value, but not so small that machine precision errors become an issue. For these simulations $U_0 = 1 \times 10^{-8}$. The domain is periodic with length 1. Electromagnetic waves do not exist in this problem, but the speed of light $c = 1$. The simulations are run to time $t = 3$ at several different resolutions and 20,000 time steps are taken for the highest resolution simulation which has 320 cells. The initial conditions for the electron x-velocity perturbation are shown in figure 3. An approximate square wave is used to excite several wave modes to test the algorithms performance effectively. A problem in the linear regime is used for two reasons. First of all, analytic solutions exist and are easy to calculate, secondly, in the linear regime the limiters can be turned off so the solution can be observed without the added dissipation which can reduce overall accuracy making it much easier to compute numerically the accuracy of the algorithm. Ultimately, problems in the non-linear regime, problems with large U_0 for example, require limiters and the overall accuracy of the numerical solution is reduced. The design of effective limiters may be the most important problem in gaining computational efficiency from 3rd order or higher discontinuous Galerkin methods for the two-fluid system when compared to the 2nd order method.

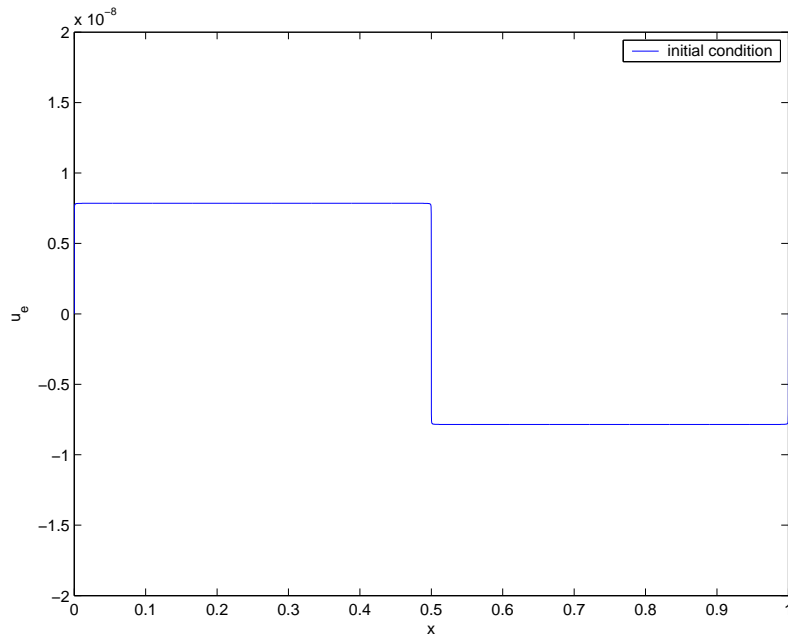


Fig. 1. Electron velocity of a square electron acoustic square pulse at time $t = 0$

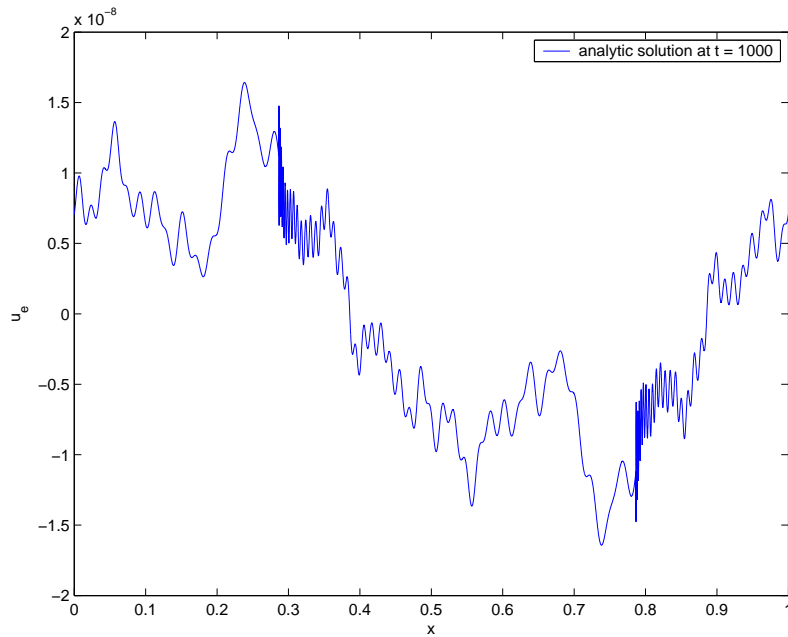


Fig. 2. Analytic solution of the electron velocity of a square electron acoustic pulse at time $t = 1000$. This plot illustrates the dispersive, non-diffusive nature of the two-fluid system that makes it numerically difficult even in the linear regime. The high frequency modes still contribute significantly to the amplitude of the solution late in time and they always will because there is no physical diffusion. The dispersive, non-diffusive nature of the two-fluid system can make it appear that our numerical solutions suffer from significant numerical dispersion errors when they are actually correctly capturing physical dispersion.

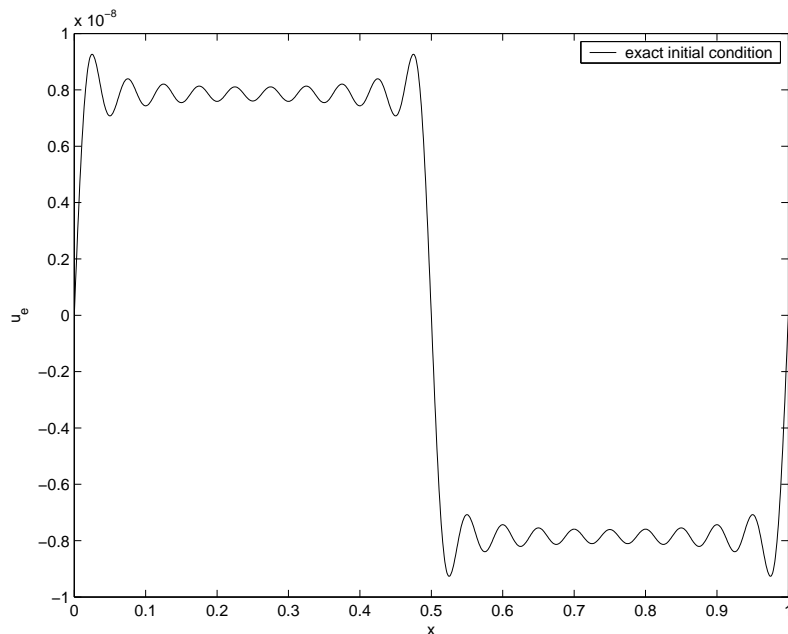


Fig. 3. Exact electron x velocity at $t=0$. Initial conditions are chosen so that all waves travel to the left as time increases. Since the waves are dispersive the initial “square wave” disappears when the solution is allowed to evolve.

After 3 time units the square pulse shape has disappeared due to wave dispersion. Plots of the numerical solution versus the analytic solution at various grid resolutions are shown in figures 4, 5, and 6 at 3 time units. In figure 4 there are 40 cells in the domain and the 3rd order method shows evidence of resolving the highest order mode. The 2nd order method only captures the bulk features. In figure 5 there are 80 cells in the domain and the 3rd order method captures the amplitude of the highest modes and matches the analytic solution very well. The 2nd order method still struggles to resolve the highest mode (note the solution at the two skinniest spikes). In figure 6 there are 160 cells in the domain and the 2nd order method still does not match the amplitude of the highest order mode and does not match the amplitudes much better than the 3rd order method at 40 grid cells. Figure 7 shows a plot of the convergence history of the numerical solutions along with calculated order of accuracy. In both cases the calculated order of accuracy varies from less than 1 for low resolution where the high frequency modes are barely resolved to better than the order of the scheme when the solution is nearly converged.

The 3rd order method performs substantially better than the 2nd order in this linearized problem when limiters are not needed. In particular, the 3rd order method preserves amplitude much better than the 2nd order, this same phenomena has been observed in certain equilibrium type non-linear problems. In general, however, the benefits of the 3rd order method over the 2nd order method for non-linear two-fluid problems is questionable. Extremely good limiters need to be developed, both to maintain accuracy and to prevent the

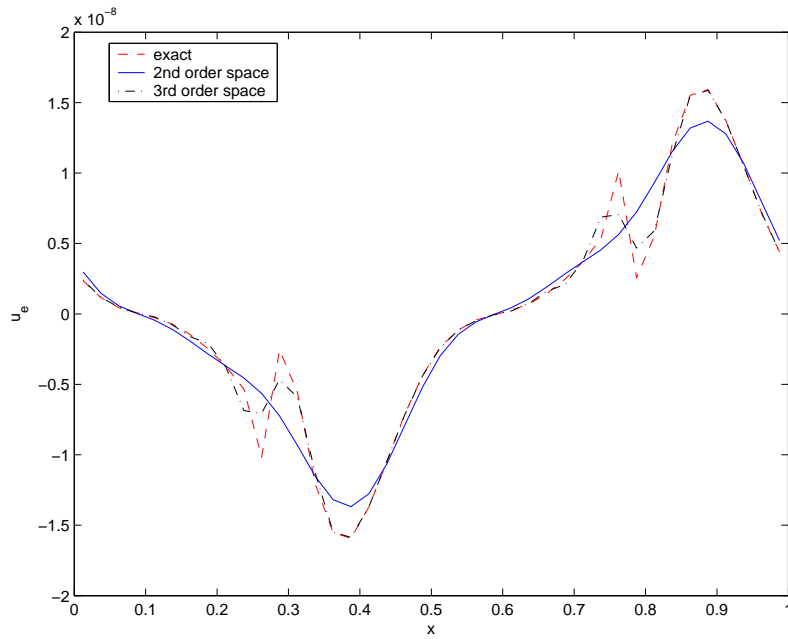


Fig. 4. Numerical solution using 2nd and 3rd order discontinuous Galerkin spatial discretizations with a 3rd order time discretization compared to the exact solution at $t=3$. The grid has 40 cells so the highest wave number mode is barely resolved with the 2nd order method. The 2nd and 3rd order solutions differ substantially from the analytic solution.

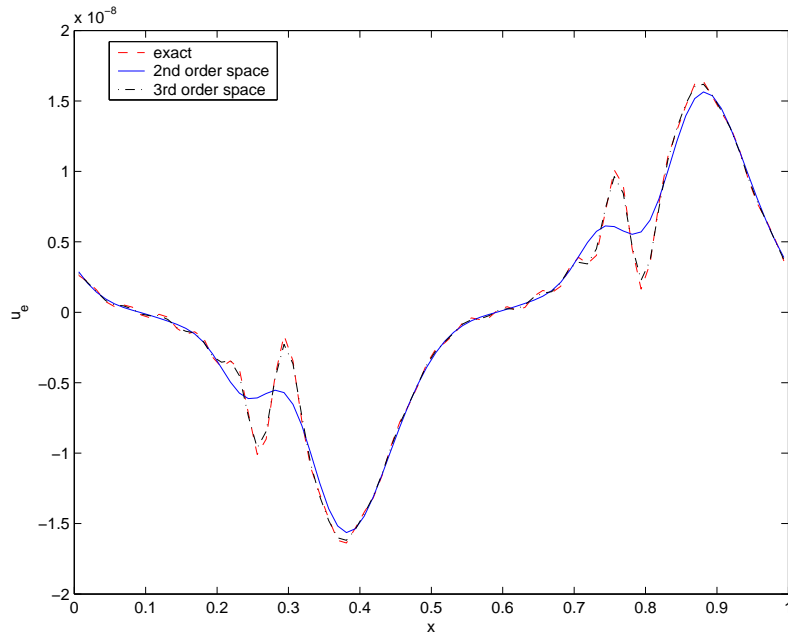


Fig. 5. Numerical solution using 2nd and 3rd order discontinuous Galerkin spatial discretizations with a 3rd order time discretization compared to the exact solution at $t=3$. The grid has 80 cells across the domain. The 2nd order solution differs substantially from the analytic solution, only capturing the lower order modes. The 3rd order solution matches the analytic solution well.

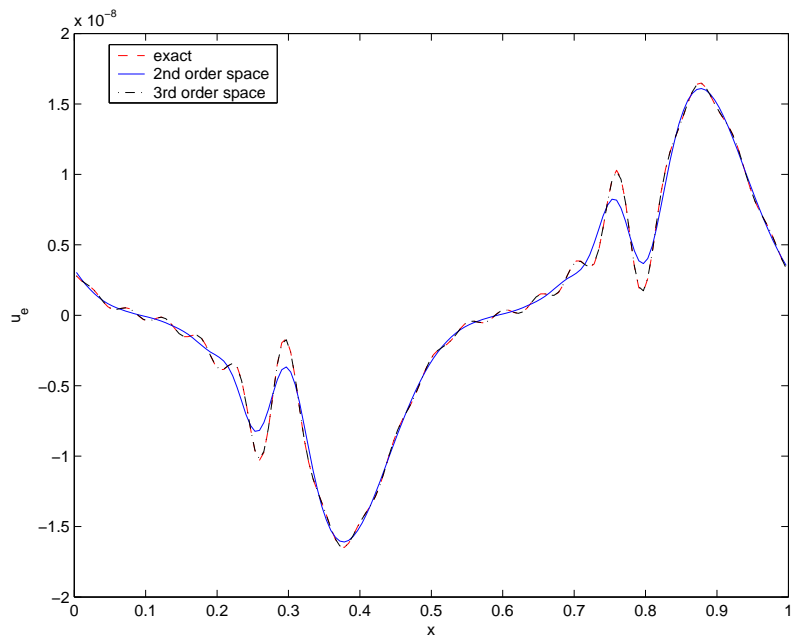


Fig. 6. Numerical solution using 2nd and 3rd order discontinuous Galerkin spatial discretizations with a 3rd order time discretization compared to the exact solution at $t=3$. The grid has 160 cells across the domain. The 2nd order solution resolves the high order modes at this resolution. At higher resolution the numerical solutions are visually indistinguishable from the analytic solution.

solution from blowing up. TVB limiters work well for some problems and a non-zero TVB constant M can be used for Maxwell's equations for all simulations, unfortunately it is much more difficult to find a non-zero M for the fluid equations that results in a stable solution, so for most problem M is simply set to 0 for the fluid equations.

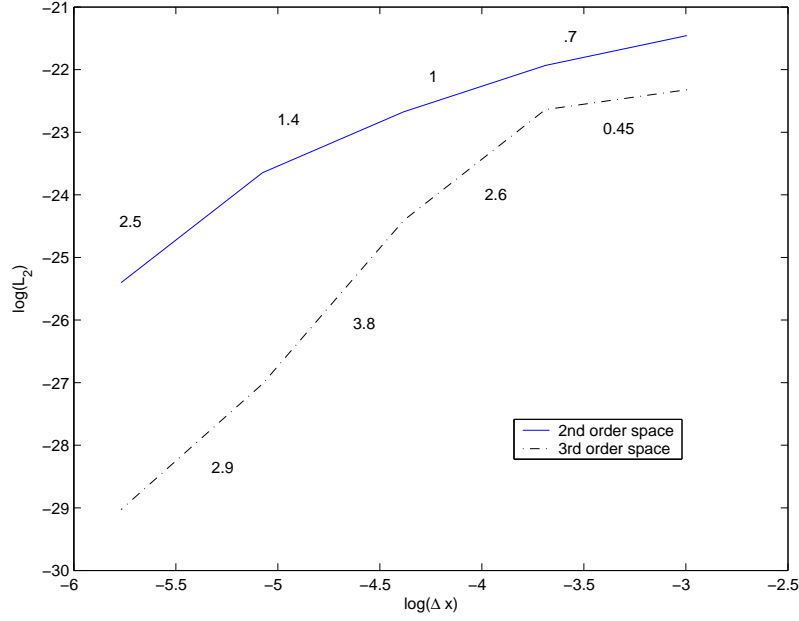


Fig. 7. Natural log of the L_2 norm versus natural log of grid spacing for the numerical solutions to the electron acoustic wave dispersion problem. The solutions were calculated using 2nd and 3rd order discontinuous Galerkin spatial discretizations with a 3rd order Runge-Kutta time discretization. The numbers near each line give the slope of the line and hence the measured order of accuracy of the scheme. The 3rd order method gives substantially better accuracy than the second order method. Grid resolutions used to construct this plot are $1/20$, $1/40$, $1/80$, $1/160$, and $1/320$. The measured accuracy was computed at $t = 3$.

5.1 Two-Fluid Electrostatic Plasma Shock

In this section we include a simulation of a simple gas dynamic shock using the two-fluid equations. The electrons and ions start out with the same discontinuous pressure and number density profile. The solution is allowed to evolve in time. The domain size is 10,000 cells in the simulation takes 200,000 time steps. An electrostatic field is quickly generated which couples the ions to the electrons. Parameters used are, $q_i = 10$, $q_e = -10$, $m_i = 1$, $m_e = \frac{1}{1836}$, $\epsilon_0 = 1$, $\mu_0 = 1$, $c = 1$, $\gamma_e = \gamma_i = \frac{5}{3}$. For a comparison, a neutral fluid with the same mass density as the ions and double the ion pressure is also included. The initial conditions are,

$$\begin{pmatrix} n_e \\ U_{ex} \\ U_{ey} \\ U_{ez} \\ P_e \\ n_i \\ U_{ix} \\ U_{iy} \\ U_{iz} \\ P_i \\ B_x \\ B_y \\ B_z \\ E_x \\ E_y \\ E_z \end{pmatrix}_{left} = \begin{pmatrix} 1.0 \\ 0 \\ 0 \\ 0 \\ 0.5 \times 10^{-4} \\ 1.0 \\ 0 \\ 0 \\ 0 \\ 0.5 \times 10^{-4} \\ 0 \\ 0 \\ 0 \\ 0 \\ 0 \\ 0 \end{pmatrix}, \quad \text{and} \quad \begin{pmatrix} n_e \\ U_{ex} \\ U_{ey} \\ U_{ez} \\ P_e \\ n_i \\ U_{ix} \\ U_{iy} \\ U_{iz} \\ P_i \\ B_x \\ B_y \\ B_z \\ E_x \\ E_y \\ E_z \end{pmatrix}_{right} = \begin{pmatrix} 0.125 \\ 0 \\ 0 \\ 0 \\ 0.05 \times 10^{-4} \\ 0.125 \\ 0 \\ 0 \\ 0 \\ 0.05 \times 10^{-4} \\ 0 \\ 0 \\ 0 \\ 0 \\ 0 \\ 0 \end{pmatrix}. \quad (42)$$

These initial conditions give a Debye length $\lambda_d = \frac{v_{the}}{w_{pe}} = 1 \times 10^{-3}$ based on the conditions on the left hand side of the domain. The electric field in the two-fluid solution couples the electron and ion pressures so that the shocks in the two-fluid solution match the location of the shocks in the neutral fluid solution. There remain significant differences in the two-fluid and neutral fluid solutions. In figure 8 spikes in ion density appear in the two-fluid solution on the Debye length scale. The spike at the shocks has a simple physical explanation and is

commonly seen in simulations of partially ionized gases[38]. The electric field increases the speed of the ion shock to match the speed of the neutral shock. The ion conditions at the ion shock still have to satisfy the Rankine Hugoniot relations, so roughly a Debye length before the shock the ions adjust their jump conditions to produce a shock that has the neutral fluid shock speed. As a result, in figure 9 a smooth rise in the ion density is seen just before the ion shock. The jump conditions at the ion shock produce a shock speed given by the neutral fluid shock speed to one percent.

The waves that appear at the base of the rarefaction wave (close up in figure 10) can be explained in a similar manner though roughly 80 percent of the magnitude of the spikes is a result of errors in Poisson's equation. The neutral rarefaction wave moves faster than the ion rarefaction wave by itself. The ion fluid attempts to undergo rarefaction before the electron fluid, when this happens an electric field develops which pulls the ion fluid density back to the electron fluid density. This process is repeated until the ions and electrons form a rarefaction wave at the same point fig.10, which also is the same point that the neutral solution rarefies at. The shocks themselves disappear if Poisson's equation is enforced and are replaced by smooth transitions.

As a practical matter these Debye length oscillations may disappear when electron-ion collisional effects or other collisional effects are included in the code; however, similar effects have been observed in simulations of partially ionized gases [38] and the existence of ion subshocks are discussed in [39] for example. Nevertheless, the analysis is important because Debye length oscillations routinely appear in two-fluid simulations and the effects are not always numerical. At the base of rarefactions, un-resolved Debye length leads to large errors in Poisson's equation and significant charge separation on a scale much greater than the Debye length; the effect is to artificially increase the Debye length. To avoid this problem, the grid spacing should approximately resolve the Debye length.

The two-fluid solution differs from the neutral solution in the pressure profile as well. In fig.11 the electron and ion pressures differ in the region between the contact discontinuity and the shock wave in such a manner that the electron pressure is decreased by roughly the same amount that the ion pressure is increased. This indicates that the pressure difference occurs because of an electric field due to charge separation, this charge imbalance begins with a negative charge bump at the base of the rarefaction and is resolved with the positive charge spike at the shock. The electric field supports a fluid pressure gradient which is exactly opposite for the electrons and ions. The pressure solution between the contact discontinuity and the shock remains unchanged when Poisson's equation is enforced, i.e., the two-temperature effect is not numerical.

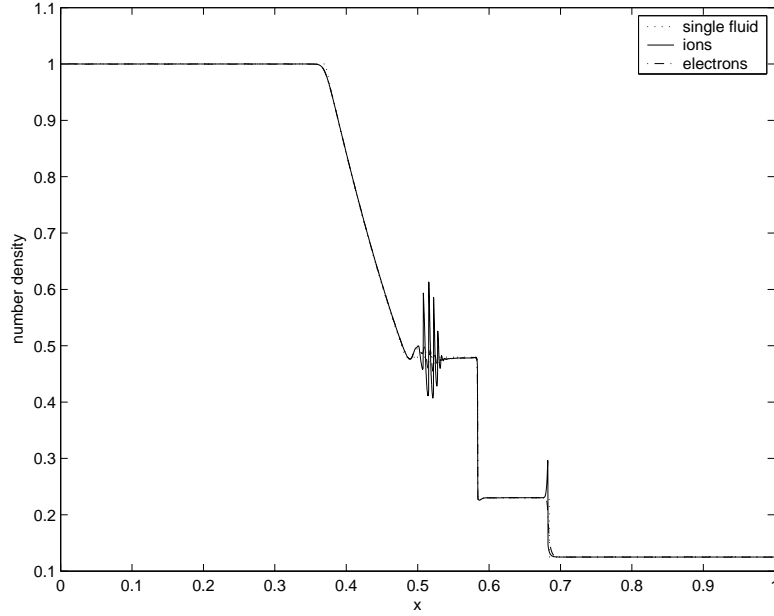


Fig. 8. Plot of number density vs position for the electron and ion fluid in comparison with a single fluid for the electrostatic plasma shock. The two-fluid equations behave much like a single fluid in this case except in the vicinity of the shocks where the ion fluid number density increases and in the region right of the rarefaction wave where similar number density variations occur. The spike at the shock remains un-changed when electric field divergence cleaning is applied, but the spikes at the rarefaction wave decrease in amplitude significantly (though never disappear) when electric field divergence cleaning is implemented.

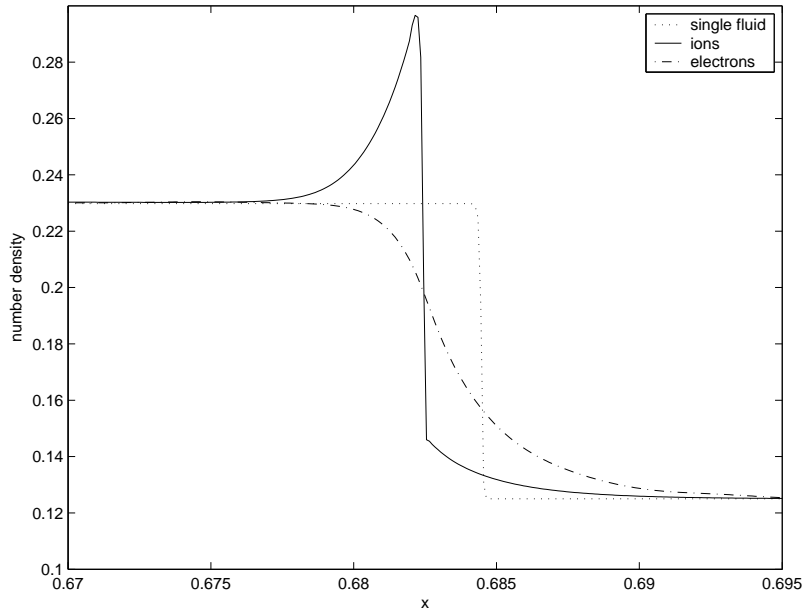


Fig. 9. Plot of number density vs position in comparison with the single fluid solution close to the shock in the electrostatic plasma shock problem. The ion fluid density increases near the shock so that the jump condition is satisfied (the solution remains unchanged when Poisson's equation is enforced). Debye shielding occurs around this spike in charge density (the Debye length is 2.4×10^{-3} in this region) and the single fluid solution lies within this Debye shielding region.

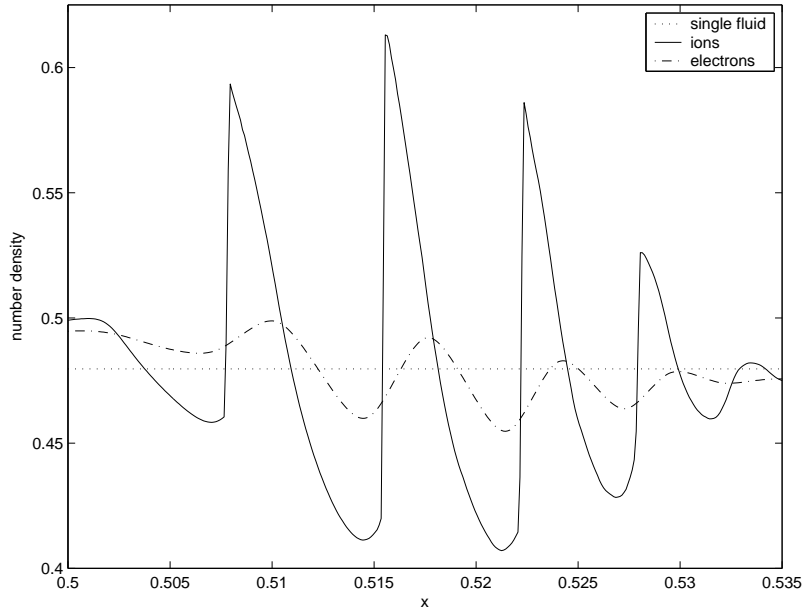


Fig. 10. Plot of two-fluid number densities compared to the single fluid solution close to the rarefaction wave in the electrostatic shock problem. The oscillations in ion density occur because the ion fluid attempts to form a rarefaction wave before the electron fluid. The result is a series of rarefaction like bumps. In the plots above, when Poisson's equation is not enforced the small rarefactions end in shock waves. When Poisson's equation is enforced the shocks disappear being replaced by a smooth transition the bumps shrink in amplitude by about 80 percent. Note that the charge separation is occurring on Debye length scales (the Debye length is 1.1×10^{-3} in this region).

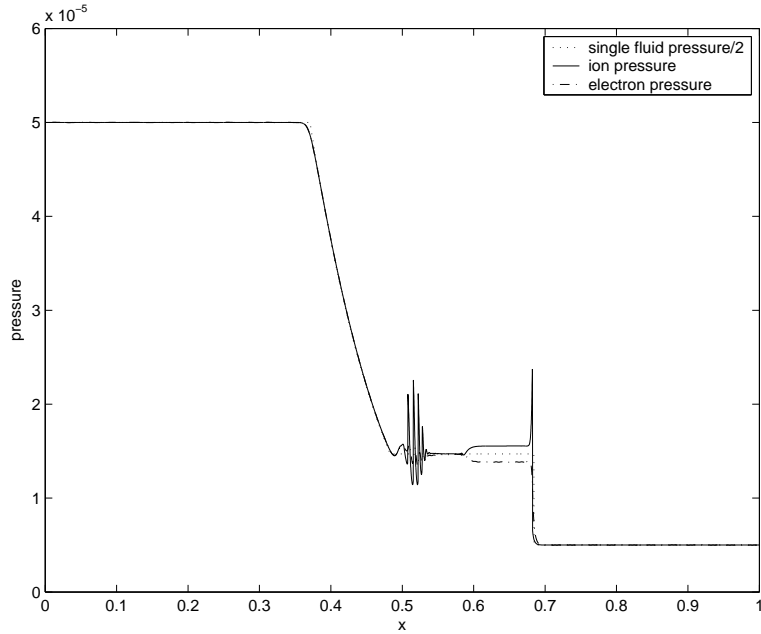


Fig. 11. Plot of pressure vs position for the electron and ion fluid in comparison with a single fluid. Notice that between the location of the contact discontinuity and the shock the electron and ion pressures are different. This pressure difference is a result of the electric field generated at the base of the contact discontinuity due to charge separation in that region. The charge separation disappears in a short distance, but the effect on the pressure remains until the shock is reached.

5.2 Two-Fluid Electromagnetic Plasma Shock

The two-fluid electromagnetic plasma shock is an extension of the Brio and Wu shock[40] to the two-fluid plasma model. The simulation was first performed in [1,41] and is used in the current paper as a benchmark. The ideal two-fluid system has no dissipative terms however an artificial viscosity exists due to the numerical discretization. Wave steepening of the two-fluid solution is limited by physical wave dispersion, when wave dispersion is not sufficient to limit the steepening, artificial viscosity limits the steepening. In real collisionless shocks in experiments and in space, kinetic effects limit the wave steepening when dispersion is not sufficient to limit the steepening. This simulation is meaningful since it illustrates the range of physics that the two-fluid system describes. These simulations were performed without enforcing Poisson's equations. Comparison with a locally gauge cleaned potential formulation show that errors in Poisson's equation do not contribute significantly to the structure of the solution. This result is somewhat surprising, since errors in Poisson's equation significantly increased the amplitude of the spikes at the base of the rarefaction wave in the case of the electrostatic shock problem.

In this paper the shock will be presented differently than in [1]. The initial dis-

continuity is allowed to evolve in time until the shock structure spans $1000r_{gi}$ where r_{gi} is the ion Larmor radius. Time is measured in terms of light transit times across the entire domain, $\tau_c = \frac{1000r_{gi}}{c}$. Snapshots of the shock earlier in time correspond to larger characteristic ion Larmor radius, $\frac{r_{gi}}{L} < 1000$ where L is the span of the shock, and so the solution evolves from a “gas dynamic” regime of short time scales and large characteristic ion Larmor radius $\frac{r_{gi}}{L} \gg 1$ to an “MHD” regime of long time scales and small characteristic Larmor radii $\frac{r_{gi}}{L} \ll 1$. Parameters used are as in the electrostatic shock, $q_i = 10$, $q_e = -10$, and $\epsilon_0 = 1$, $\mu_0 = 1$, $c = 1$, $\gamma_e = \gamma_i = \frac{5}{3}$, $m_i = 1$, $m_e = \frac{1}{1836}$. The initial conditions on the left half of the domain are given by,

$$\begin{pmatrix} n_e \\ U_{ex} \\ U_{ey} \\ U_{ez} \\ P_e \\ n_i \\ U_{ix} \\ U_{iy} \\ U_{iz} \\ P_i \\ B_x \\ B_y \\ B_z \\ E_x \\ E_y \\ E_z \end{pmatrix}_{left} = \begin{pmatrix} 1.0 \\ 0 \\ 0 \\ 0 \\ 0.5 \times 10^{-4} \\ 1.0 \\ 0 \\ 0 \\ 0 \\ 0.5 \times 10^{-4} \\ 0.75 \times 10^{-2} \\ 1.0 \times 10^{-2} \\ 0 \\ 0 \\ 0 \\ 0 \end{pmatrix}, \quad \text{and} \quad \begin{pmatrix} n_e \\ U_{ex} \\ U_{ey} \\ U_{ez} \\ P_e \\ n_i \\ U_{ix} \\ U_{iy} \\ U_{iz} \\ P_i \\ B_x \\ B_y \\ B_z \\ E_x \\ E_y \\ E_z \end{pmatrix}_{right} = \begin{pmatrix} 0.125 \\ 0 \\ 0 \\ 0 \\ 0.05 \times 10^{-4} \\ 0.125 \\ 0 \\ 0 \\ 0 \\ 0.05 \times 10^{-4} \\ 0.75 \times 10^{-2} \\ 1.0 \times 10^{-2} \\ 0 \\ 0 \\ 0 \\ 0 \end{pmatrix}. \quad (43)$$

The spatial units of figures 12, 13, 14 are measured in ion Larmor radii r_{gi} based on the initial conditions in the left half of the domain. The Debye length is $\lambda_d = \frac{1}{100} r_{gi}$ also based on the initial conditions on the left half of the domain. The results in figure 12 are virtually identical to those published in [1] figure 8. The domain of figure 12 has only 500 cells (5,000 time steps to reach this point in the simulation) while the published solution has 4000 cells in the domain. Increasing the resolution of the simulation at this scale produces additional high frequency waves which are “superimposed” on the solution presented and do not change the results significantly. In figure 13 the solution begins to

deviate more from the previously published solution in figure 9 of [1] as can be seen by the oscillations to the left of the rarefaction wave. At this scale there are 5000 cells in the domain (50,000 time steps to reach this point in the simulation) while there are 4000 cells in the previously published solution. The waves to the left of the rarefaction wave decay due to numerical diffusion; the shortest wavelengths decaying most. With increased resolution the decay can be reduced, but additional shorter wave lengths are resolved which also decay rapidly in amplitude. At the final time figure 14, the solution has moved beyond those published and significant oscillations to the left of the shock are observed. The magnitude of the waves to the left of the rarefaction wave have continued to decay compared to their magnitude in figure 13, once again, due to numerical diffusion. The oscillations are dispersive magnetosonic waves and are a feature of laminar collisionless shocks [42]. Most of these waves are resolved in several hundred grid cells, and the entire domain of figure 14 is 50,000 cells (500,000 time steps to reach this point in the simulation). At this resolution the number of oscillations behind the shock remains constant with further refinement and the solution is converged with the caveat that higher wave number modes will continue to appear, superimposed on the solution presented, as the grid is refined further - (recall, this same issue is illustrated in the discussion of the electron acoustic square pulse simulations).

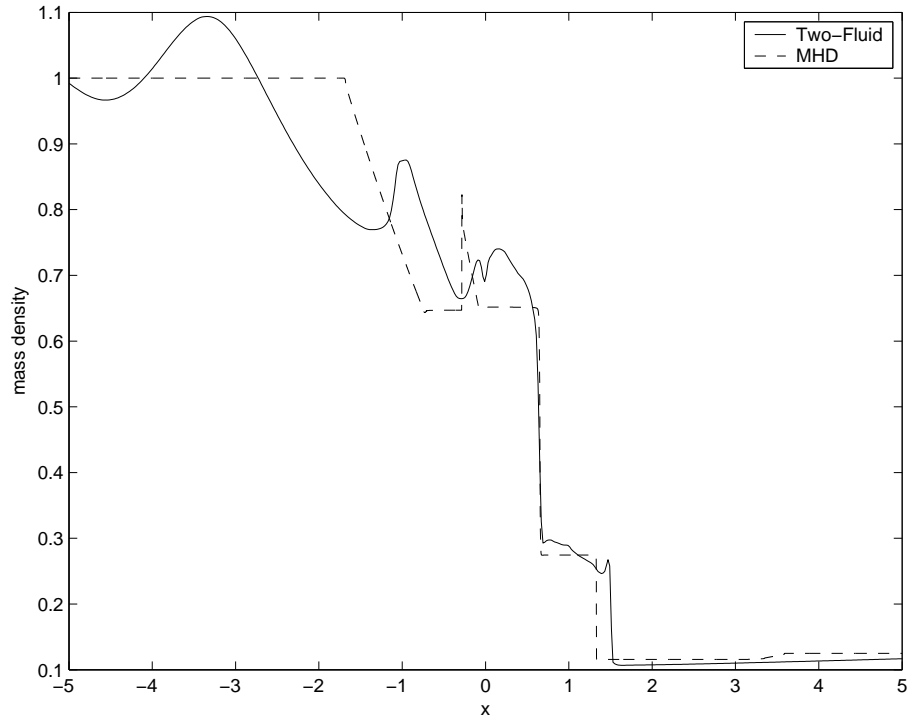


Fig. 12. Electromagnetic shock solution using the two-fluid equations and the MHD equations at $t = 0.01\tau_c$. At this time the domain spans 10 ion Larmor radii or 1000 Debye lengths. It is in this regime that the two-fluid solution differs most significantly from the MHD or the “gas dynamic” solution. This regime may also have practical applications to Z-Pinches and FRC’s.

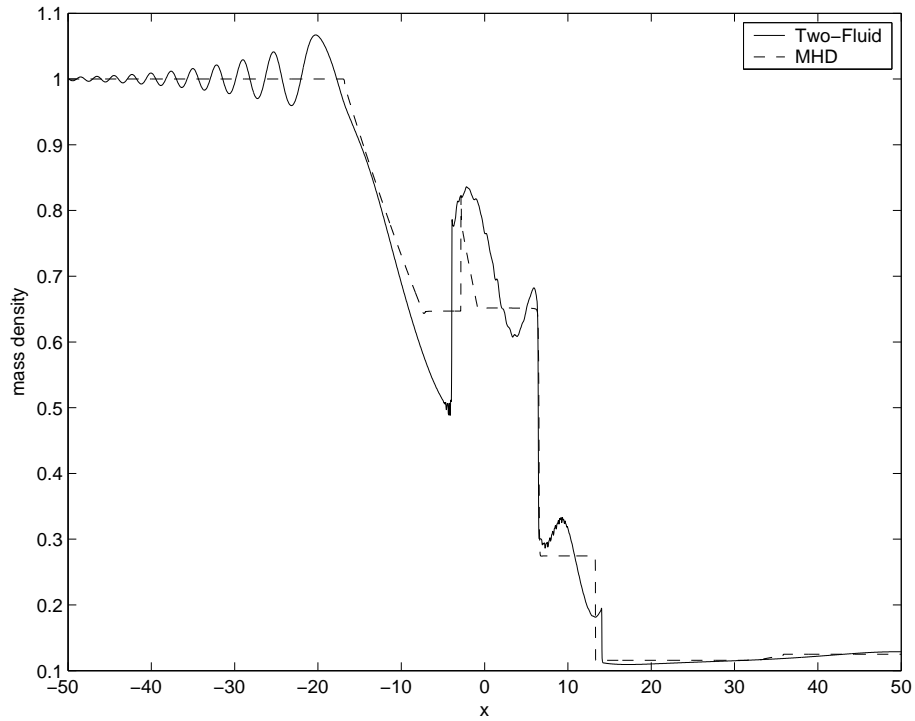


Fig. 13. Electromagnetic shock solution using the two-fluid equations and the MHD equations at $t = 0.1\tau_c$. At this time the domain spans 100 ion Larmor radii or 10000 Debye lengths. Major differences from previously published results include the large oscillations to the left of the rarefaction wave which are dispersive magnetosonic waves.

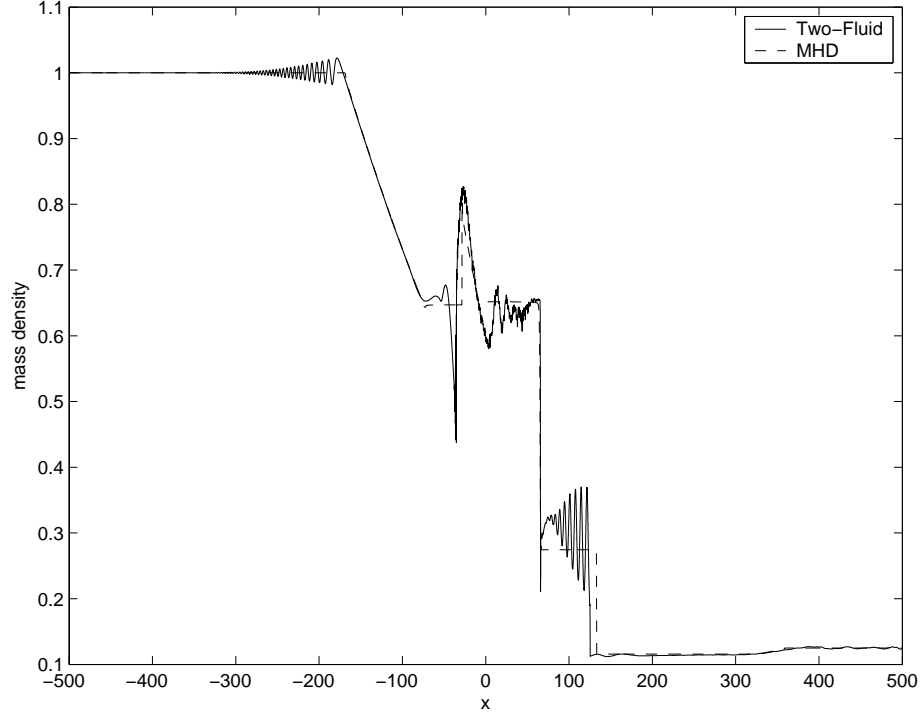


Fig. 14. Electromagnetic shock solution using the two-fluid equations and the MHD equations at $t = 1\tau_c$. At this point in the simulation the solution is very MHD like. However, key differences remain and there is no indication that these differences will subside with increased resolution or further time evolution. The most major differences are the post shock and post rarefaction wave oscillations. Both look numerical, but these waves are resolved in several hundred grid cells and are believed to be dispersive magnetosonic waves. The exponential decay in these waves is a result of the numerical diffusion of the algorithm. Higher resolution runs show more high frequency waves with less diffusion, but essentially the same results.

In ideal MHD the fluid is frozen to the magnetic field lines and this prevents one field line from connecting with another because as two field lines are pushed together the fluid forces act to push the lines apart. The addition of non-ideal terms which allow the fluid to move across field lines, such as resistivity, allows the magnetic reconnection process to occur. However, classical resistivity leads to much slower reconnection rates than are observed in collisionless space and fusion plasmas where there is effectively no resistivity. Non-ideal, collisionless terms are responsible for the fast reconnection that is observed to occur in the earth's magnetotail and fusion plasmas. In this section we show that the two-fluid algorithm developed in this paper produces magnetic reconnection rates that agree with those described of the GEM challenge magnetic reconnection problem as described in [2].

The GEM challenge magnetic reconnection problem is non-dimensionalized as in [2] where lengths are normalized by the ion inertial length $d = c/w_{pi} = c \left(\frac{e^2 n_0}{\epsilon_0 m_i} \right)^{-\frac{1}{2}}$ time is non-dimensionalized by the ion-cyclotron time $\frac{m_i}{e B_0}$ where B_0 is the magnetic field at infinity. The velocities are normalized by the Alfvén velocity $V_a = \left(\frac{B_0^2}{\mu_0 m_i n_0} \right)^{\frac{1}{2}}$. Finally current density is non-dimensionalized by $J_0 = \frac{B_0 w_{pi}}{\mu_0 c}$ and E by $E_0 = V_a B_0$. The domain is $(-6.4 d, 6.4 d)$ and the simulation is run out to $40/w_{ci}$. Conducting walls are used on the y boundaries and periodic boundaries are used on the x boundaries. $\lambda = 0.5 d$, the ion to electron mass ratio is taken to be 25 and the specific heat ratio $\gamma = \frac{5}{3}$. The speed of light is $c = 10 V_a$. The reconnection rates do not change noticeably when the ratio of the speed of light to the Alfvén speed is increased to $c = 100 V_a$ as was done in [43]. The initial number densities are given by,

$$n_e = n_i = n_0 \left(\frac{1}{5} + \operatorname{sech}^2 \left(\frac{y}{\lambda} \right) \right). \quad (44)$$

The electron and ion temperatures differ slightly, but are constant throughout the domain, this gives the following electron pressure, P_e ,

$$P_e = \frac{1}{12\mu_0} B_0^2 \frac{n_e}{n_0} \quad (45)$$

and ion pressure P_i

$$P_i = \frac{5}{12\mu_0} B_0^2 \frac{n_i}{n_0}. \quad (46)$$

The electron and ion pressure balance the magnetic field which is given by

$$B_x = B_0 \tanh \left(\frac{y}{\lambda} \right) + \frac{B_0}{10} \frac{\pi}{L_x} \cos \left(\frac{2\pi x}{L_x} \right) \sin \left(\frac{\pi y}{L_y} \right) \quad (47)$$

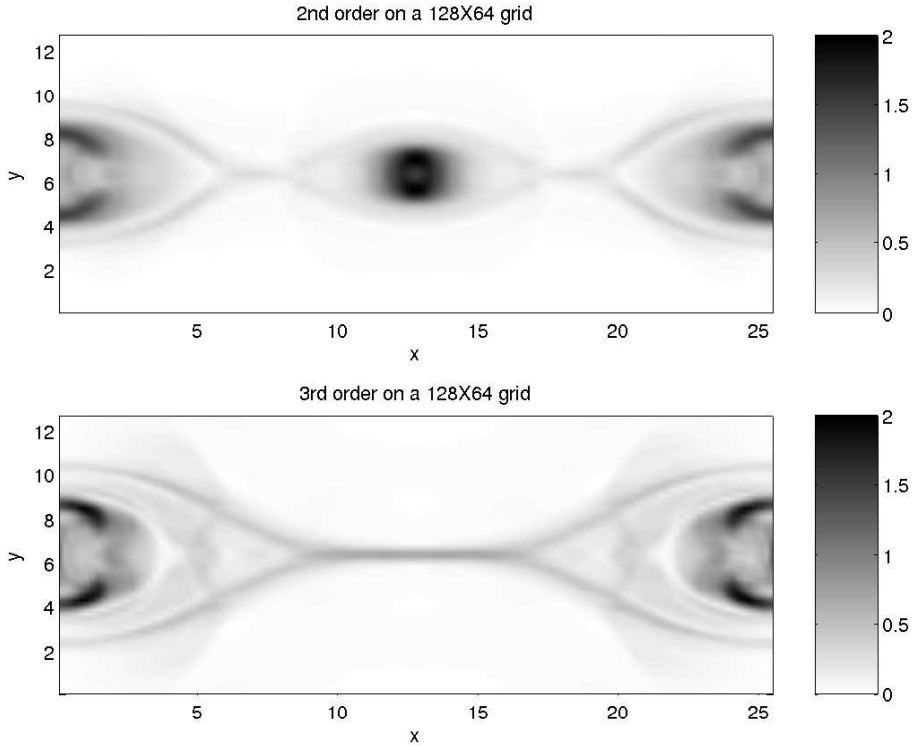


Fig. 15. GEM challenge comparing $|J_z|$ using the 2nd and 3rd order method on a 128×64 grid at time $t = 25/w_{ci}$. At this resolution an island forms in the 2nd order method and grows as the simulation progresses. Both methods use 3rd order TVD Runge-Kutta time stepping.

$$B_y = \frac{B_0}{10} \left(\frac{2\pi}{L_x} \right) \sin \left(\frac{2\pi x}{L_x} \right) \cos \left(\frac{\pi y}{L_y} \right) \quad (48)$$

The magnetic field is in equilibrium with with the electron current J_{ze} ,

$$J_{ze} = \frac{\mu_0 B_0}{\lambda} \operatorname{sech}^2 \left(\frac{x}{\lambda} \right). \quad (49)$$

The simulations are run at two resolutions, 128×64 and 512×256 using a second or third order discontinuous Galerkin method with third order TVD Runge Kutta time stepping. At a resolution of 512×256 , 80 thousand time steps are taken and at a resolution of 128×64 , 20 thousand time steps are taken. In figure 15 low resolution solutions to the GEM challenge problem are plotted at $t = 25/\omega_{ci}$. The second order solution shows stable island formation while in the third order method no island forms. In this simulation the TVB limiter constant $M = 0$ is used to eliminate the formation of an unstable island in the third order method. Solutions to the GEM challenge problem are highly susceptible to bifurcation [44] which is the formation of magnetic islands at or near the x-point (the center of the domain in this case). This problem has been observed in many algorithms including our divergence free finite volume algorithm so that magnetic islands can develop even without

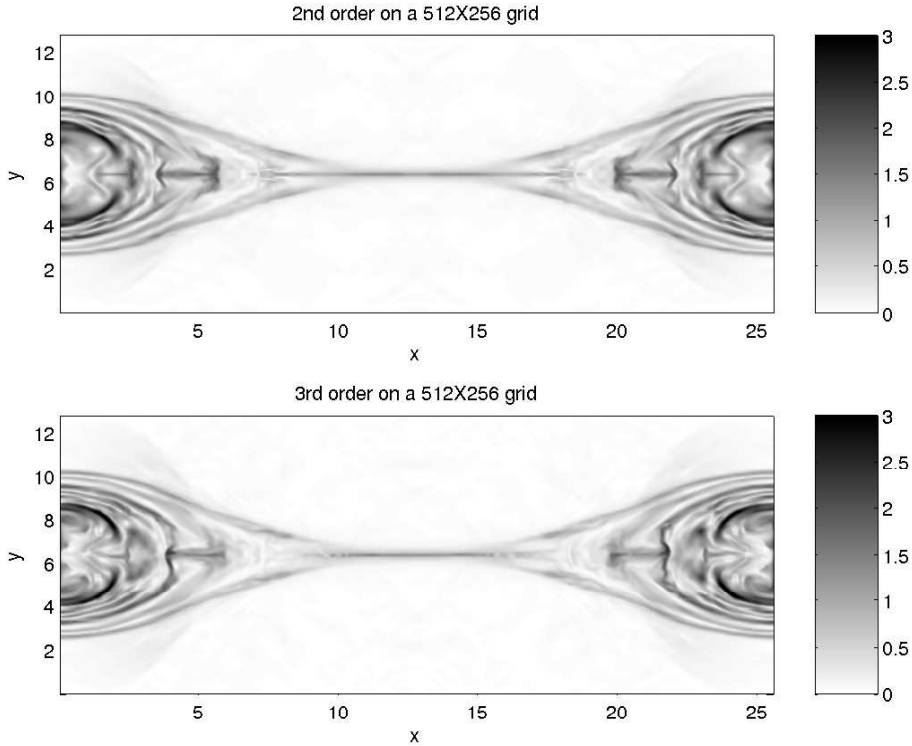


Fig. 16. GEM challenge comparing $|J_z|$ using the 2nd and 3rd order method on a 512×256 grid at time $t = 25/\omega_{ci}$. At this resolution the 2nd and 3rd order method look similar. Both methods use 3rd order TVD Runge-Kutta time stepping. Instabilities develop out of the fluid jets that emerge from the x-point when they collide with the slow moving fluids in the lobes.

divergence errors. The development of these islands may be due to excessive dissipation applied at the x-point; however, the development of islands can be unpredictable and in the case of the 3rd order method, increased dissipation can actually eliminate the island.

Physically the development of islands is unstable and any small perturbation in the location or fields in the island will cause the island to slip and merge with one of the lobes. Small perturbations can arise from machine precision error and this is particularly true at locations near equilibrium where two nearly equal but opposing forces are added, the number that remains may depend significantly on the precision of the numbers used. It has been observed that increasing machine precision can change the direction that an unstable island slips off to. The second order solution shows the formation of a stable island presumably due to the extra dissipation of the second order method.

In figure 16 the high resolution solutions are plotted at $t = 25/\omega_{ci}$ with the TVB limiter constant $M = 25$. At this resolution the second and third order methods produce very similar results. In this case no island formation is visible in either the second or third order schemes, however at time $t = 30/\omega_{ci}$ a very

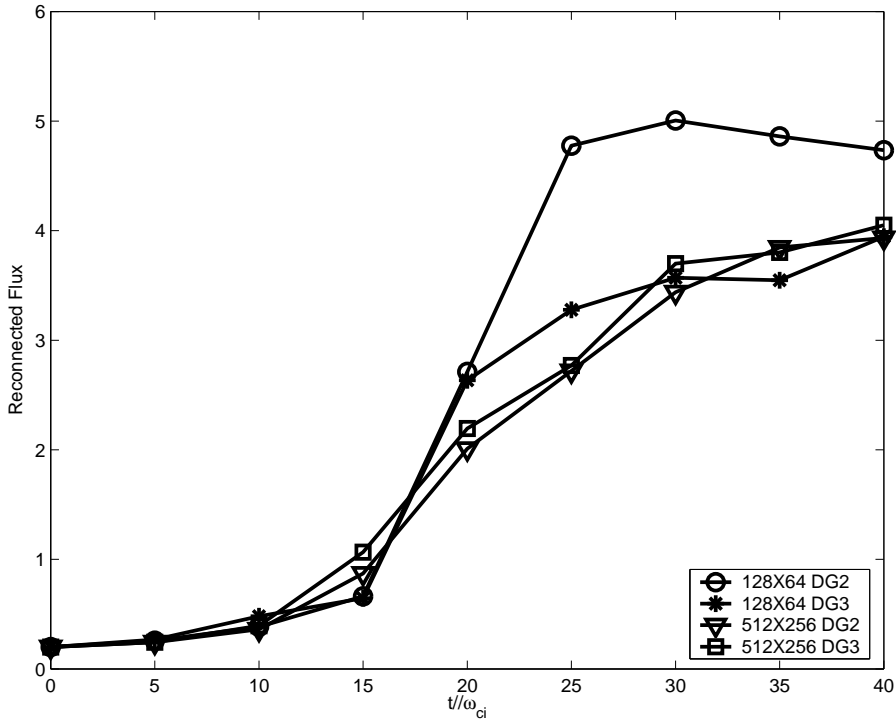


Fig. 17. Plot of reconnected flux vs time for 2nd and 3rd order spatial discretizations at resolutions of 128×64 and 512×256 . The reconnected flux differs substantially for the two methods at 128×64 , though the 3rd order method better matches the high order solutions. At 512×256 the 2nd and 3rd order methods are in close agreement.

small unstable island forms in the 3rd order method and combines with the left lobe before $t = 35/\omega_{ci}$. If a less diffusive flux function such as an approximate Riemann flux is used in the second order method, unstable islands will form. In figure 17 the reconnected magnetic flux $\frac{1}{2} \int |B_y| dx$ along the x axis is plotted for several solutions. At grid resolution of 512×256 the second and third order methods produce similar results. At a resolution of 128×64 the third order method produces results which are in much better agreement with the high resolution results than does the second order method. In figure 18 the solution using the 3rd order discontinuous Galerkin method with 3rd order TVD Runge-Kutta time stepping is compared with solutions produced with particle, hybrid and Hall MHD codes in [45]. The two-fluid solution agrees with all the converged solutions until near the point of saturation. Physically, the reconnected solution must eventually saturate. In figure 19 the reconnected flux up to time $t = 60/\omega_{ci}$ is shown illustrating the saturation of the numerical solution beyond the published time interval in the GEM challenge results [2].

Flows appear late in time which are turbulent as shown in figure 20 at time $t = 40/\omega_{ci}$. The 3rd order method shows considerably more asymmetry than the 2nd order method, but asymmetry has begun to develop in the 2nd order solution. This asymmetry develops out of machine precision errors that

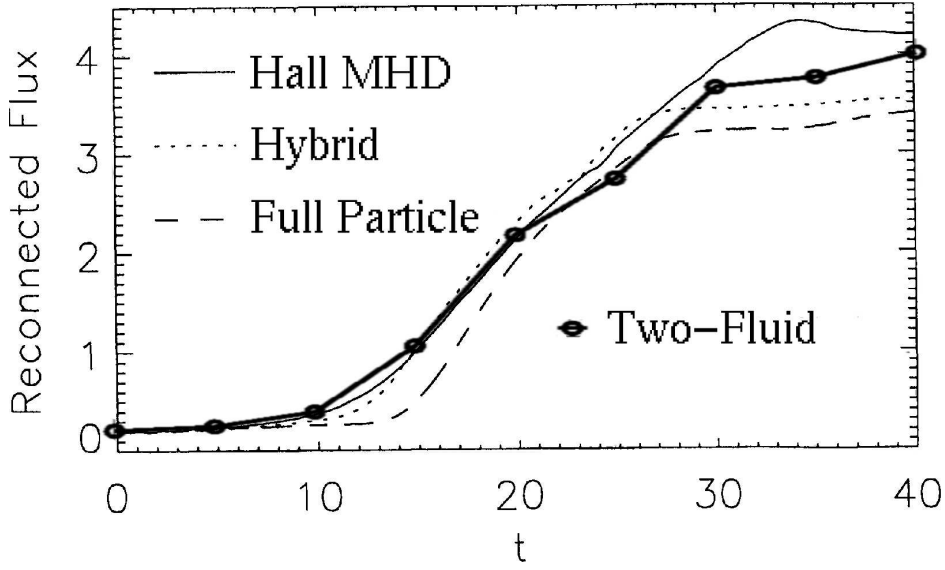


Fig. 18. Comparison of the two-fluid solution using the 3rd order discontinuous Galerkin method with TVD 3rd order Runge-Kutta time stepping vs previously published solutions in [45]. This plot was taken from [45] and the two-fluid solution superimposed on top. The two-fluid solution shows good agreement with the other methods. The Hall MHD code uses a term which depends on electron mass and thus differs from other published Hall MHD solutions where the electron mass is taken to be 0.

are initiated in the current layer at the x -point from the balancing of source terms and fluxes. The only dissipation present is numerical so the second order method tends smooth out the errors produced by the finite precision more than the 3rd order method. As a result of the low dissipation in the 3rd order method these errors result in the excitation of unstable modes which eventually effect the macroscopic solution. The magnitude of electron momentum can differ by as much as 10 percent by moving from 64 bit numbers to 80 bit numbers at $t = 40/\omega_{ci}$; fortunately these regions tend to be localized.

Notice the pair of shocks in figure 20, the positions differ in the two solutions. The positions differ because the onset of the fast growth stage is slightly different for the two methods. As the fast growth begins, shocks form in the ion fluid as it is accelerated along the x axis. Eventually the two jets of shocked ion fluid collided and two shock that spans the y axis are formed which continues to propagate through the domain as the solution evolves. If the onset of fast growth differs slightly initially, then these shocks will appear at different locations for a given time.

In figure 21 percent magnetic field jump due to divergence errors are plotted. The field jumps are measured against the magnetic field at infinity B_0 . The

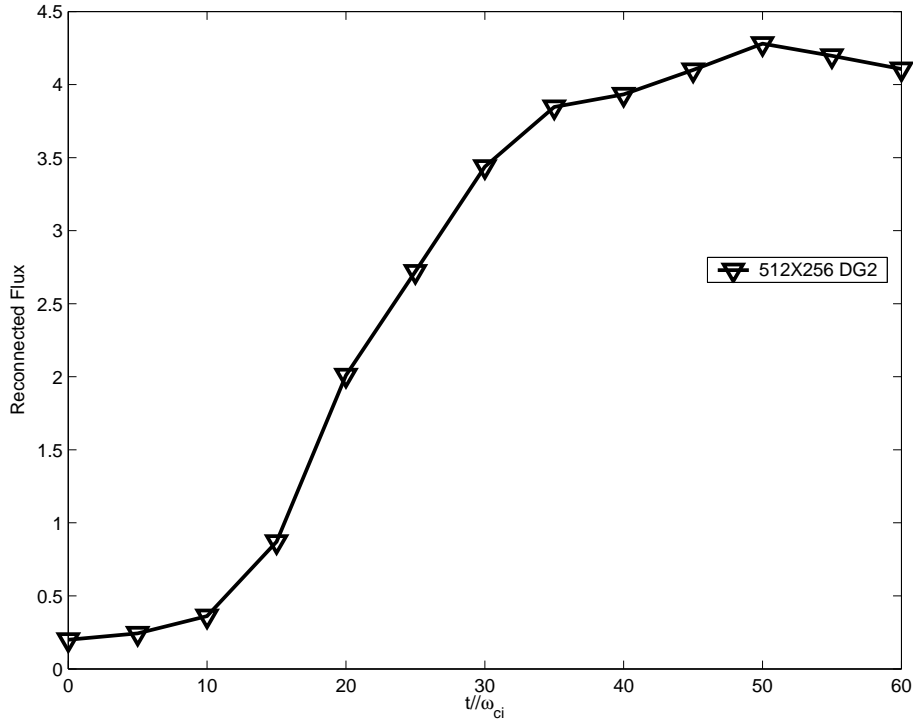


Fig. 19. Plot of reconnected magnetic flux to time $t = 60/\omega_{ci}$ for a 512X256 solution. This figure shows that the two-fluid solution does saturate as would be expected with conducting walls and finite flux in the domain.

magnetic field jump is defined for each cell in regular geometry as,

$$B_{jump} = \sum_{faces} B \cdot n, \quad (50)$$

where n is the normal to the face. This condition gives the increase or decrease in magnetic field strength in each cell due to errors in the divergence constraint. The results in figure 21 show that the magnetic field jumps remains fairly small even at $t = 40/\omega_{ci}$. In the 2nd order method on the 512X256 grid the divergence errors are grid aligned. Ultimately, divergence cleaning needs to be implemented in the numerical method, in this problem however, magnetic field divergence errors remain small and divergence errors are not visible at all at the shocks.

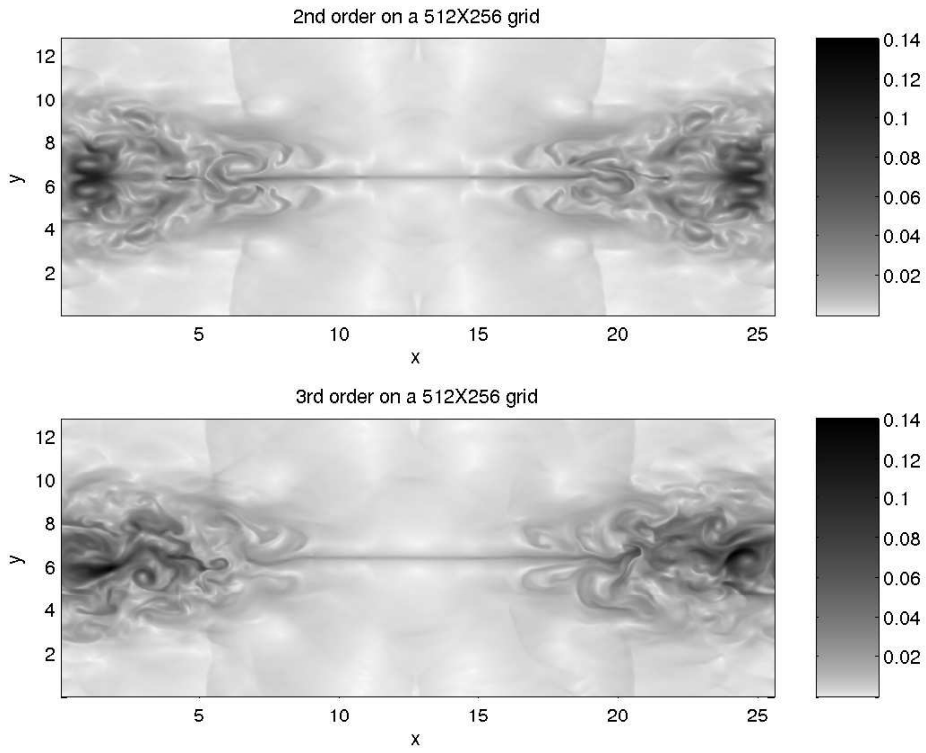


Fig. 20. Plot of total ion momentum at $t = 40/\omega_{ci}$ at a resolution of 512×256 using the second and third order DG methods.

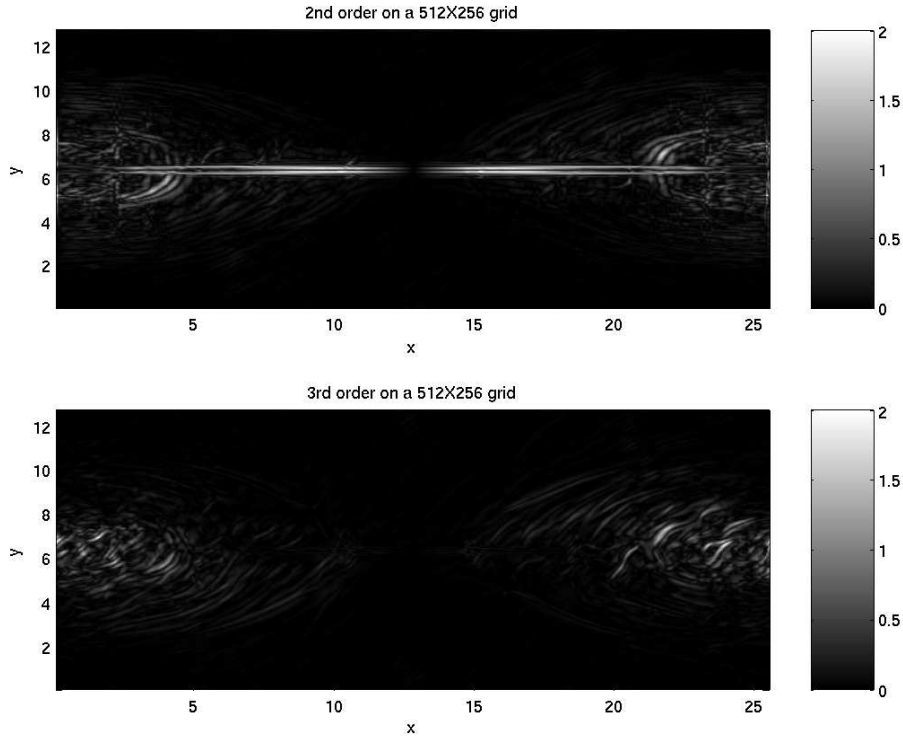


Fig. 21. Percent magnetic field jump due to divergence errors based on the B field at infinity $B_0 = 0.1$ at $t = 40/\omega_{ci}$ at a resolution of 512×128 using the second and third order DG methods. The 2nd order solution peaks at 2% while the 3rd order solution peaks at 3%. The divergence errors in the 3rd order solution are much more localized despite the greater maximum error. The second order solution shows grid aligned divergence errors.

6 Discussion

A discontinuous Galerkin method for the ideal 5-moment two-fluid plasma system is developed. A scalar model problem of the ideal two-fluid system is derived to illustrate the character of the full system. An analytic two-fluid solution to an electron acoustic square pulse in the linear regime is derived and the numerical solution using the fully non-linear two-fluid system is calculated showing convergence for the 2nd and 3rd order discontinuous Galerkin methods. An electrostatic gas-dynamic shock problem is presented to illustrate the existence of Debye length oscillations and Debye length ion shocks in two-fluid solutions and to give a physical interpretation. The algorithm is benchmarked against the two-fluid electromagnetic shock originally published in [1]. The 2nd and 3rd order algorithms are tested on the GEM challenge magnetic reconnection problem and produces results comparable to those generated by particle codes, hybrid codes, and a Hall MHD code. The issue of computational efficiency of the 3rd order method is an open question. Improved limiters would significantly improve the 3rd order solution and should be investigated. The discontinuous Galerkin method offers a straight forward method for solving the ideal 5-moment two-fluid system. This same algorithm could be applied to 10 and higher moment two-fluid systems so that various kinetic effects can be simulated inside the fluid framework. Divergence free, or divergence cleaning electromagnetics techniques discussed in [21] can easily be applied to the algorithm developed in this paper. The algorithm can be easily generalized to three dimensions and general geometries.

References

- [1] U. Shumlak, J. Loverich, Approximate riemann solver for the two-fluid plasma model, *Journal of Computational Physics* 187 (2003) 620–638.
- [2] J. Birn, et al., Geospace environmental modeling (gem) magnetic reconnection challenge, *Journal of Geophysical Research* 106 (A3) (2001) 3715–3719.
- [3] J. P. Freidberg, *Ideal Magnetohydrodynamics*, Plenum Press, 1987.
- [4] P. M. Bellan, *Spheromaks*, Imperial College Press, 2000.
- [5] J. W. Connor, Pressure gradient turbulent transport and collisionless reconnection, *Plasma Physics and Controlled Fusions* 35 (1993) 757–763.
- [6] N. A. Krall, P. C. Liewer, Low-frequency instabilities in magnetic pulses, *Physical Review A* 4 (5) (1971) 2094–2103.
- [7] R. C. Davidson, N. T. Gladd, Anomalous transport properties associated with the lower-hybrid-drift instability, *The Physics of Fluids* 18 (10) (1975) 1327–1335.

- [8] L. Solovév, Dynamics of a cylindrical z pinch, *Soviet Journal of Plasma Physics* 10 (5) (1984) 602–605.
- [9] M. Haines, The physics of the dense z-pinch in theory and in experiment with application to fusion reactor, *Physica Scripta T2/2* (1982) 380–390.
- [10] O. S. Jones, U. Shumlak, D. S. Eberhardt, An implicit scheme for nonideal magnetohydrodynamics, *Journal Of Computational Physics* 130 (1997) 231–242.
- [11] C. Sovinec, et al., Nonlinear magnetohydrodynamics simulation using high-order finite elements, *Journal of Computational Physics* 195 (2004) 355–386.
- [12] A. Bhattacharjee, Center for magnetic reconnection studies: Present status, future plans, PSACI PAC Presentation, Princeton (June 2003).
- [13] J. Breslau, S. Jardin, A parallel algorithm for global magnetic reconnection studies, *Computer Physics Communications* 151 (2003) 8–24.
- [14] J. D. Huba, Hall magnetohydrodynamics - a tutorial, in: M. S. J. Buchner, C.T. Dunn (Ed.), *Space Plasma Simulation*, Springer, 2003, pp. 166–192.
- [15] W. Park, et al., Plasma simulation studies using multilevel physics models, *Physics of Plasmas* 6 (5) (1999) 1796–1803.
- [16] S. Baboolal, Finite-difference modeling of solitons induced by a density hump in a plasma multi-fluid, *Mathematics and Computers in Simulation* 55 (2001) 309–316.
- [17] R. Schneider, C. D. Munz, The approximation of two-fluid plasma flow with explicit upwind schemes, *International Journal of Numerical Modelling: Electronic Networks, Devices and Fields* 8 (1995) 399–416.
- [18] P. Rambo, J. Denavit, Time-implicit fluid simulation of collisional plasmas, *Journal Of Computational Physics* 98 (1991) 317–331.
- [19] R. Mason, An electromagnetic field algorithm for 2d implicit plasma simulation, *Journal of Computational Physics* 71 (1987) 429–473.
- [20] R. Mason, C. Cranfill, Hybrid two-dimensional electron transport in self-consistent electromagnetic fields, *IEEE Transactions on Plasma Science* 14 (1) (1986) 45–52.
- [21] A. Hakim, J. Loverich, U. Shumlak, A high resolution wave propagation scheme for ideal two-fluid plasma equations, Submitted to the *Journal of Computational Physics*.
- [22] B. Cockburn, C.-W. Shu, Tvb runge-kutta local projection discontinuous galerkin finite element method for conservation laws ii: General framework, *Mathematics of Computation* 52 (1989) 411–435.
- [23] B. Cockburn, S.-Y. Lin, C.-W. Shu, Tvb runge-kutta local projection discontinuous galerkin finite element method for conservation laws iii: One-dimensional systems, *Journal of Computational Physics* 84 (1989) 90–113.

- [24] B. Cockburn, S. Hou, C.-W. Shu, The runge-kutta local projection discontinuous galerkin finite element method for conservation laws iv: Multidimensional case, *Mathematics of Computation* 54 (1990) 545–581.
- [25] B. Cockburn, C.-W. Shu, The runge-kutta discontinuous galerkin method for conservation laws v: Multidimensional systems, *Journal of Computational Physics* 141 (1998) 199–224.
- [26] J. S. Hesthaven, T. Warburton, Nodal high-order methods on unstructured grids, *Journal of Computational Physics* 181 (2002) 186–221.
- [27] B. Cockburn, F. Li, C.-W. Shu, Locally divergence-free discontinuous galerkin methods for maxwell’s equations, *Journal of Computational Physics* 194 (2004) 588–610.
- [28] T. C. Warburton, G. E. Karniadakis, A discontinuous galerkin method for the viscous mhd equations, *Journal of Computational Physics* 152 (1999) 608–641.
- [29] A. Mangeney, F. Califano, C. Cavazzoni, P. Travnicek, A numerical scheme for the integration of the vlasov-maxwell system of equations, *Journal of Computational Physics* 179 (2002) 495–538.
- [30] B. Cockburn, G. E. Karniadakis, C.-W. Shu (Eds.), *Discontinuous Galerkin Methods*, Springer, 2000.
- [31] B. nan Jiang, J. Wu, L. A. Povinelli, The origin of spurious solutions in computational electromagnetics, *Journal Of Computational Physics* 125 (1996) 104–123.
- [32] D. Durran, *Numerical Methods for Wave Equations in Geophysical Fluid Dynamics*, Springer, 1998.
- [33] B. Cockburn, Discontinuous galerkin methods for convection-dominated problems, in: *High-Order Methods for Computational Physics*, Springer, 1999.
- [34] R. J. LeVeque, *Finite Volume Methods for Hyperbolic Problems*, Cambridge University Press, 2002.
- [35] R. Biswas, K. D. Devine, J. E. Flaherty, Parallel, adaptive finite element methods for conservation laws, *Applied Numerical Mathematics* 14 (1994) 255–283.
- [36] G. Toth, The divb constraint in shock-capturing magnetohydrodynamics codes, *Journal Of Computational Physics* 161 (2000) 605–652.
- [37] C. D. Munz, R. Schneider, U. Vos, A finite-volume method for the maxwell equations in the time domain, *Siam Journal of Scientific Computing* 22 (2000) 449–475.
- [38] R. Rubinstein, A. Auslender, Non-ideal gas effects on shock waves in weakly ionized gases, Tech. rep., ICASE (2000).

- [39] C. Kennel, J. Edmiston, T. Hada, A quarter century of collisionless shock research, in: *Collisionless Shocks in the Heliosphere: A Tutorial Review*, AGU, 1985, pp. 1–36.
- [40] M. Brio, C. C. Wu, An upwind differencing scheme for the equations of ideal magnetohydrodynamics, *Journal Of Computational Physics* 75 (1988) 400–422.
- [41] J. Loverich, A finite volume algorithm for the two-fluid plasma system in one dimension, Masters thesis, University of Washington (2003).
- [42] K. Papadopoulos, Microinstabilities and anomalous transport, in: *Collisionless Shocks in the Heliosphere: A Tutorial Review*, AGU, 1985, pp. 59–90.
- [43] J. Loverich, U. Shumlak, A discontinuous galerkin method for the full two-fluid plasma model, *Computer Physics Communications* 169 (2005) 251–255.
- [44] M. Hesse, J. Birn, M. Kusnetsova, Collisionless magnetic reconnection: Electron processes and transport modeling, *Journal of Geophysical Research* 106 (2001) 3721–3735.
- [45] M. A. Shay, J. F. Drake, B. N. Rogers, R. E. Denton, Alfvénic collisionless magnetic reconnection and the hall term, *Journal of Geophysical Research* 106 (2001) 3759–3772.